UNIVERSITÀ
DEGLI STUDI
DI PADOVA

SEDE AMMINISTRATIVA: UNIVERSITÀ DEGLI STUDI DI PADOVA

DIPARTIMENTO DI SCIENZE CHIMICHE

CORSO DI DOTTORATO IN SCIENZE MOLECOLARI

CURRICULUM: SCIENZE CHIMICHE

CICLO: XXXI

SURFACE SUPPORTED SUPRAMOLECULAR ARCHITECTURES: AN EXPERIMENTAL AND MODELING STUDY

COORDINATORE DEL CORSO: CHIAR.MO PROF. LEONARD JAN PRINS

SUPERVISORE: CHIAR.MO PROF. MAURIZIO CASARIN

DOTTORANDA: ELAHEH MOHEBBI

Abstract

Surface Supported Supramolecular Architectures:
An Experimental and Modeling study

L’auto-organizzazione di molecole organiche su superfici solide è uno degli approcci più diffusi per la creazione di architetture supramolecolari supportate di dimensioni controllate e con proprietà innovative. L’uso combinato di differenti interazioni di natura non covalente adsorbato–adsorbato e adsorbato–substrato consente infatti la modulazione dell’associazione di specie distinte in modo quasi altrettanto accurato che nei sistemi biologici, fonte primaria di ispirazione per ciò che può essere realizzato artificialmente. Il consenso sull’uso d’interazioni intermolecolari estese non covalenti nell’ingegnerizzazione di nanostrutture bidimensionali supportate prive di difetti è unanime. Ciononostante, i materiali così ottenuti sono spesso fragili, incapaci di resistere a condizioni aggressive, privi di stabilità meccanica ed inefficienti nei processi di trasferimento di carica intermolecolare; sono cioè materiali inadatti per applicazioni tecnologiche. La produzione di sistemi nanostrutturati supportati con proprietà predeterminate, privi di difetti e con risvolti applicativi implica quindi la sintesi di *network* covalenti robusti, non caratterizzati dalle limitazioni di cui sopra. In questa tesi di dottorato si è voluta esplorare sia sperimentalmente sia teoricamente la possibilità di stabilizzare covalentemente *network* supramolecolari funzionali in una/due dimensioni stimolando la formazione di legami covalenti tra molecole preorganizzate su una superficie.

Abstract

Surface Supported Supramolecular Architectures:
An Experimental and Modeling study

The scientific community is nowadays focused on the design and the production of nm/μm-sized systems for their relevance to nanotechnology, energy production and storage, life science and environment. Advances in high performing computing and in synthetic/characterization methods make possible devising novel rational approaches to tailor properties of low-dimensional architectures of molecular networks on inorganic substrates; i.e., to control the electron transport properties of active layers and the reactivity of selected sites. As such, the self-assembly of functional architectures on appropriate surfaces is the most promising bottom-up approach to organize and integrate single molecules on solid substrates. As a consequence of the persistent progress in computational power and multiscale material modeling, new materials are less likely to be discovered by a trial-and-error approach. This points to a paradigm shift in modeling, away from reproducing known properties of known materials and towards simulating the properties of hypothetical composites as a forerunner to get real materials with desired characteristics. The interplay among multiscale material modeling, new synthetic routes and appropriate validation experiments is crucial to design the desired behavior at each length scale. In this PhD thesis we exploited integrated methodologies to provide interpretative tools about structure and functions of organic/inorganic hybrid nanostructured materials made of molecular mono-layers deposited on technological relevant substrates, suitable for applications in strategic areas such as catalysis, artificial photosynthesis, molecular electronics-magnetism and molecular recognition.

Table of Contents

II

List of Figures

List of Tables

Glossary

1,2-bis(4-bromophenyl)ethyne	DBPE
2,3,5,6-tetraoxyquinone	TOQ
Atomic Orbital	AO
Bond length	BL
Bridge	B
Brillouin-zone	BZ
Covalent Organic Framework	COF
Density Functional Theory	DFT
Exchange-Correlation	XC
Free	F
Face Centered Cubic	FCC
Fast Fourier Transform	FFT
Full Charge Density	FCD
Generalized Gradient Approximation	GGA
Graphene Nanoribbon	GNR
High Temperature	HT
Highest occupied molecular orbital	HOMO
Hartree & Fock	HF
Hohenberg & Kohn	HK
Hollow	H
Kohn & Sham	KS
Local Density Approximation	LDA
Low-energy electron-diffraction	LEED
Long-range	LR
Low Temperature	LT
Lowest unoccupied molecular orbital	LUMO
Metal-Organic Framework	MOF
Metallo Phthalocyanine	MPc
Metal Porphyrin	MP
Molecular Orbital	MO
Monolayer	ML
Møller-Plesset	MPn

Mustiscale Materials Modeling	MMM
Oligo(aryleneethynylenes)	OAE
On-Surface-Synthesis	OSS
One-Dimensional	1D
Poly(aryleneethynylenes)	PAE
Polyconjugated Aromatic Hydrocarbon	PAH
Perdew Burke Ernzerhof	PBE
Poly(phenyleneethynylene)	PPE
Poly(ParaPhenylene)	PPP
Quantum ESPRESSO	QE
Room Temperature	RT
Self-Assembly	SA
Scanning Tunnelling Microscopy	STM
Schrödinger Equation	SE
Secondary Building Unit	SBU
Self-Assembly	SA
Short-range	SR
Surface Covalent Organic Framework	SCOF
Tersoff-Hamann	TH
Thomas & Fermi	TF
Three-Dimensional	3D
Tetrahydroxyquinone	THQ
Top	T
Two-Dimesional	2D
Ullmann Coupling	UC
Ultra-High Vacum	UHV
van der Waals	vdW
X-ray Photoelectron Spectroscopy	XPS
Zero-Dimensional	0D

Introduction

Despite the growing computing power has augmented our capability of modeling the details of physico-chemical processes, we still face the challenge that phenomena of interest are often the result of interactions between multiple spatial and temporal scales, and processes of interest are necessarily treated by means of substantially different models at different scales. With specific reference to the condensed matter, the researchers' attention is focused on the properties of systems whose length scale extends over ~10 orders of magnitude, ranging from ~1 nm to macroscopic functional components in materials engineering. Surely, physics provides basic theories and modeling strategies to treat matter at all scales; nevertheless, there is no single and all-including model to compute material properties at all scales relevant for materials science, where complex structural hierarchies occurring in nature are often mimicked by artificial chemical and engineering devices. At the sub-nanometric scale there are only atoms; however, at larger scales, they generate complex hierarchical structures, which have to be treated with different theories, each one having a certain range of applicability [Steinhauser, 2008]. In this regard, computational modeling of materials behavior is becoming a reliable tool to underpin scientific investigations and to complement traditional theoretical and experimental approaches. In fact, multiscale theories recognize that interesting phenomena often takes place at multiple length scales simultaneously, and their ultimate purpose is the one of including the theoretical description of these different length scales into a single framework. With specific reference to the material modeling, multiscale material modeling (MMM) aims to enhance predictive materials research by combining advanced materials theory with principles of computational science. MMM is thus not only an evolution of the traditional materials modeling field; rather, it represents a revolution in this

field because of the possibility of developing frameworks to tackle materials modeling problems at multiple time and length scales in unifying ways. As a part of the wider field of materials science, MMM is necessarily interdisciplinary and intimately linked to experiments, thus playing the dual role of improving our understanding of materials and enabling the design of new materials with boosted performances. From an experimental point of view, since the Grill's seminal study on on-surface-synthesis (OSS) in UHV [Grill et al., 2007] through thermally-triggered covalent linking of halogenated organic precursors (Ullmann Coupling – UC;) [Ullmann & Bielecki, 1901], the scientific community has witnessed a growing experimental activity aimed to go "beyond supramolecular self-assembly" [Gourdon, 2008]. Conventional self-assembly techniques, either by condensation in vacuum or by precipitation from solution, represent viable routes to synthesize artificial homo- and hetero-molecular architectures; however, most of them are typically stabilized through weak van der Waal's (vdW) interactions easily broken under operation conditions. The stabilization of one dimensional (1D)/two dimensional (2D) organic frameworks requires either the immobilization of the organic active centers by chemical linking to specific surface sites or the optimization of bottom-up synthetic routes to tailor robust, well-defined, covalent organic framework (COF) on inorganic substrates starting from well-designed secondary building units (SBUs) [Gourdon, 2008; Franc & Gourdon, 2011]. The interest for these 1D/2D materials lies in the issues they raise about their electronic, transport and magnetic properties exploitable for optoelectronic devices, sensing, bioimaging, molecular electronics and, if spin-bearing precursors are integrated in the nanostructures, single molecule magnet-based spintronics [Bogani & Wernsdorfer, 2008]. A huge range of reactions beyond the UC has been adapted to UHV OSS to produce 1D/2D materials, and particular efforts have been devoted to the synthesis of polymers affording π-conjugation in 2D [Gutzler & Perepichka, 2013; Perepichka & Rosei, 2009] to match the unique transport properties of graphene with the need of a non-vanishing band-gap, necessary in most electronic device applications and affordable through a proper SBUs functionalization. Polyconjugated aromatic hydrocarbons (PAHs) and heteroaromatic dyes have been also effectively exploited in thin film technology to tailor their anisotropic properties (e.g. transport) through an appropriate choice of the substrate geometry and structure. As such, PAHs require a suitable peripheral

functionalization to establish a chemical bonding with substrates, while metallorganic dyes, such as porphyrins and phthalocyanines, offer a larger number of degrees of freedom to tailor the adsorbate-substrate interaction. In this regard, it is noteworthy that a large number of experimental evidences concur to demonstrate that the electronically active center can be directly involved in chemical reactions with the substrate and that, more specifically, the incorporation of metal atoms from the substrate [González-Moreno et al., 2011], predeposited clusters [Gottfried et al., 2006; Kretschmann et al., 2007] or post-growth deposition [Marbach, 2015] can now be considered an OSS routine protocol to produce ultrapure ordered films of metalloporphyrins (MPs). As such, it has been demonstrated in the near past that the self-metalation reaction can be favored by the presence of surface oxygen on metals [Verdini et al., 2016]. Direct self-metalation on transition metal oxides (TMOs), such as rutile TiO (110), represents one step forward to the strengthening of the molecule to substrate interaction since it leads to the formation of the most robust porphyrin overlayer reported so far (stable up to 450 °C) [Lovat et al., 2017]. A further popular approach for the COFs' synthesis is the one implying the boronic group, which can undergo condensation upon either auto-recognition process (three boronic terminations link to form a boroxine group) or hetero-recognition with catechol [Kubo et al., 2015]. On surfaces, boronic 2D COFs may be obtained with good morphology both in solution and in UHV [Clair et al., 2014; Guam et al., 2012] and have been successfully employed as templates for the growth of molecular films [Plas et al., 2016]. Moreover, it has been recently shown that the boroxine ring can promote ultrafast charge transfer towards the metallic electrode [Toffoli et al., 2017], suggesting that the boronic templates may not only drive the morphology of complex hybrid interfaces but may also have an active role in defining their electronic properties. OSS has been also recently exploited to produce molecular devices by manufacturing hybrid systems realized by anchoring suitable molecular architectures on previously functionalized technological substrates. As such, covalent mono and multi-layers of structurally organized metal-organic networks have been recently prepared, consisting of Os or redox-active Ru complexes able to generate supramolecular networks exhibiting reversible redox reactions and showing useful electrochemical properties [Kumar et al., 2014]. Finally, the great flexibility of free porphyrins and MPs, fullerenes, and some Rh complexes has been exploited in the near past to produce a variety of functional materials, such as memory elements,

photovoltaic systems, switches and sensors.

Research in this field has been so far mostly based on synthetic advancements and a trial-and-error approach, and no unified computational framework exists for a rational design of these systems. This PhD thesis is meant to provide a contribution in the modeling of surface supported self-assembled architectures. To this end, two case studies will be considered: i) the surface-confined 2D polymerization of the 1,2-bis(4-bromophenyl)ethyne on Ag(110); ii) the generation of a metallorganic coordination network of tetrahydroxyquinone on Cu(111). Molecular and electronic structure of adsorbates and of the adsorbate/substrate interfaces will be modeled by running DFT calculations as implemented in the Quantum ESPRESSO (QE) suite [Giannozzi et al., 2009]. Moreover, original scanning tunneling microscopy (STM) maps of the surface supported 1D/2D supramolecular architectures will be simulated within the Tersoff-Hamann (TH) approach [Tersoff & Hamann, 1985]. The pivotal role played in this thesis by the theoretical modeling has been twice: on one hand, it provided an irreplaceable tool to rationalize experimental evidences; on the other hand, it drove experiments towards the desired outcomes, in a sort of cross-fertilization successfully experimented in the past by the group in which the thesis has been developed.

Chapter 1

Theoretical Framework, Basis Theories and Concepts

1.1 The Schrödinger Equation

In quantum mechanics (QM) the physical state of a quantum system (e.g., atoms, molecules and extended systems) can be completely described, at a given moment, by a definite (in general complex) function, the so-called wave function. Such a function is the solution of the time-dependent Schrödinger equation [Schrödinger, 1926a-g], the fundamental equation of QM, which describes the changes of a quantum state with time:

$$i\hbar\frac{\partial\Psi(t)}{\partial t}=\hat{H}\Psi(t) \qquad (1.1.1)$$

where $\hat{H}$ is the Hamiltonian operator describing the total energy of the system of interest, and $\Psi(t)$ is the time-dependent wave function. When $\hat{H}$ does not depend explicitly on time, it coincides with the total energy operator and it corresponds to the sum of kinetic and potential energy operators. In general, the form of the Hamiltonian operator defines the solution of the wave equation and so the wave function, as solution of the following eigenvalue equation:

$$\hat{H}\Psi_i=\varepsilon_i\Psi_i \qquad (1.1.2)$$

where the eigenvalue ε_i is the energy associated to the i-th eigenstate Ψ_i of the chemical system. Thus, the definition of the Hamiltonian operator is a problem of primary importance. Moreover, it is worth of note that the eigenstates of the Hamiltonian $\hat{H}$ are orthogonal by definition and form a complete basis set in the Hilbert space of the system. The wave function itself has not a precise physical meaning, but its square is associated to the probability of finding the particle described by the wave function at a given point and time. In particular, for an atomic or molecular system with N electrons the electron density ρ is related to the square of the modulus of the wave function, $|\Psi|^2$, and it is defined as:

$$\rho(\boldsymbol{r}) = N \int d\boldsymbol{r}_2\, d\boldsymbol{r}_3 \ldots d\boldsymbol{r}_N \left|\Psi(\boldsymbol{r}_2, \boldsymbol{r}_3, \ldots, \boldsymbol{r}_N)\right|^2 \tag{1.1.3}$$

For the validity of the Eq. (1.1.3), the wave functions must be normalized accordingly to

$$\left\langle \Psi_i \middle| \Psi_j \right\rangle = \delta_{ij} \tag{1.1.4}$$

where δ_{ij} is the Kronecker delta, to let the electron density ρ to integrate the total number of electrons N:

$$\int \rho(\boldsymbol{r})\, d\boldsymbol{r} = N \tag{1.1.5}$$

In a non-relativistic approach, the Hamiltonian operator for a chemical system with N electrons (i, j, . . .) and M nuclei (p, q, . . .) with Zp, Zq, . . . charges can be written (in atomic units)* as:

$$\hat{H} = -\frac{1}{2m_p}\sum_{p=1}^{M}\hat{\nabla}_p^2 - \frac{1}{2}\sum_{i=1}^{N}\hat{\nabla}_i^2 - \sum_{p,i}^{M,N}\frac{Z_p}{r_{ip}} + \sum_{p<q}^{M,M}\frac{Z_p Z_q}{R_{pq}} + \sum_{i<j}^{N,N}\frac{1}{r_{ij}} \tag{1.1.6}$$

* In Hartree atomic units, the numerical values of the following four fundamental physical constant are all unity by definition: electron mass m_e ($9^{.10938188(72)} \times 10^{-31}$ kg); elementary charge e ($1.602176462(63) \times 10^{-19}$ C); reduced Planck's constant $\hbar$ ($1.054571596(82) \times 10^{-34}$ J•s); Coulomb's constant $k_e = (4\pi\varepsilon_0)^{-1}$ (8.987551787×10^9 N•m^2•C^{-2}) [Lide, 2009].

where the first and second terms are the kinetic energies of the nuclei and electrons, respectively, the third is the Coulomb electron-nucleus attractive interaction, and the fourth and the fifth terms are the Coulomb nucleus-nucleus and electron-electron repulsions, respectively. However, for most chemical applications, the electronic and nuclear motions can be separated as a consequence of the huge difference between the electron and the nuclei masses, and the Hamiltonian can be written as a sum of nuclear and electronic contributions. This is known as Born-Oppenheimer approximation [Born & Oppenheimer, 1927] according to which the Hamiltonian of the quantum system can be rewritten in terms of the electronic one:

$$\hat{H}_e = -\frac{1}{2}\sum_{i=1}^{N}\hat{\nabla}_i^2 - \sum_{p,i}^{M,N}\frac{Z_p}{r_{ip}} + \sum_{i<j}^{N,N}\frac{1}{r_{ij}} \qquad (1.1.7)$$

where the nuclear coordinates are treated as constants, and the nuclear repulsion (the fourth term of the right-hand side (RHS) of Eq. (1.1.6)) can be considered as a constant value for each nuclear configuration r_{pq}. The first term of the electronic Hamiltonian of equ. (1.1.7) corresponds to the kinetic energy operator for the N electrons ($\hat{T}_e$), the second is the nucleus-electron Coulomb interaction ($\hat{V}_{ne}$) on the i^{th} electron due to the M nuclei (each of them characterized by a charge Z_p) and the third term is the electron-electron repulsion ($\hat{V}_{ee}$). Interestingly, the Eq. (1.1.7) shows that the actual system of interest is involved in the Hamiltonian through the position and the nature of its nuclei and the total number of electrons N. If is Ψ is known, the expectation value of any physical quantity can be defined as [Landau & Lifshitz, 1965]:

$$\left\langle \hat{A} \right\rangle = \frac{\int \Psi^* \hat{A} \Psi d\tau}{\int \Psi^* \Psi d\tau} = \frac{\left\langle \Psi \middle| \hat{A} \middle| \Psi \right\rangle}{\left\langle \Psi \middle| \Psi \right\rangle} \qquad (1.1.8)$$

where $\hat{A}$ is the linear Hermitian operator[†] associated to the physical quantity A. In particular, if the wave function Ψ is normalized, the expectation values for the kinetic

[†] An operator $\hat{A}$ is Hermitian or self-adjoint if $\hat{A}^\dagger = \hat{A}$. Eigenvalues of Hermitian operators are real; moreover, corresponding eigenvectors are orthogonal [Landau & Lifshitz, 1965].

and the potential energies are

$$T\left[\Psi\right]=\left\langle \hat{T}\right\rangle =\int \Psi^{*}\hat{T}\Psi d\tau \tag{1.1.9}$$

and

$$V\left[\Psi\right]=\left\langle \hat{V}\right\rangle =\int \Psi^{*}\hat{V}\Psi d\tau \tag{1.1.10}$$

where the square brackets indicate that T and V are two distinct functional of Ψ.

1.2 The Thomas – Fermi Model

The density functional theory stems from the Thomas & Fermi (TF) model [Thomas, 1927; Fermi, 1927; Fermi, 1928; Wigner, 1934; Weizsäcker, 1935; Lieb, 1981; March, 1986; Perdew & Wang, 1986; Koch & Holthausen, 2001; Tsuneda, 2014], according to which the quantum state of a uniform free electron gas in three dimensions can be described by its electronic density ρ_0 instead of the wave function. The electron density can be expressed as function of the Fermi momentum p_f (Ashroft et al., 1976), which is defined for the highest energy one-electron occupied level as:

$$p_f = \hbar k_f \tag{1.2.1}$$

$$k_f = \left(\frac{3\pi^2 N}{V_f} \right)^{\frac{1}{3}} \tag{1.2.2}$$

where k_f is the *Fermi wave vector*, N is the number of electrons and V_f is the spherical momentum space volume. The corresponding energy

$$\varepsilon_f = \frac{\hbar^2 k_f^2}{2m} \tag{1.2.3}$$

is the *Fermi energy* [Kittel, 2005]. So the electron density ρ_0 for a uniform electron gas is:

$$\rho_0 = \frac{p_f^3}{3\pi^2 \hbar^3} \tag{1.2.4}$$

This formulation, exact for a uniform electron gas, has been then extended to inhomogeneous electron densities, such as those characterizing atoms, molecules and solids in the presence of an external potential $\upsilon(\boldsymbol{r})$. If the inhomogeneous electron density at the point $\boldsymbol{r}$ is denoted by $\rho(\boldsymbol{r})$, when the equation defining ρ_0 is applied locally at $\boldsymbol{r}$, the expression for the total electronic energy is

$$E_{\mathrm{TF}}\left[\rho(\boldsymbol{r})\right] = C_{\mathrm{TF}}\int d\boldsymbol{r}\rho^{\frac{5}{3}}(\boldsymbol{r}) + \int d\boldsymbol{r}\upsilon(\boldsymbol{r})\rho(\boldsymbol{r}) + \frac{1}{2}\iint d\boldsymbol{r}_1 d\boldsymbol{r}_2 \frac{\rho(\boldsymbol{r}_1)\rho(\boldsymbol{r}_2)}{|\boldsymbol{r}_2 - \boldsymbol{r}_1|} \quad (1.2.5)$$

where C_{TF} is a constant corresponding to

$$C_{\mathrm{TF}} = \frac{3}{10}\left(3\pi^2\right)^{\frac{2}{3}} \quad (1.2.6)$$

the first term of the RHS of Eq. (1.2.5) is the kinetic energy of the electrons, the second is the attraction between the electrons and the nucleus and the third term accounts for the inter-electronic repulsion. The important result they reached was that the total electronic energy for a system with N electrons, E[ρ], could be expressed as a functional, E_{TF}, of the charge density $\rho(\mathbf{r})$. The revolutionary aspect of this approach is that, for the first time, the ground-state energy of a system is a functional of a physical observable like the electron density, and not a functional of the wave function, which does not correspond to a physical observable. Eq. (1.2.5) is an approximate form of the rigorous expression for the electronic energy (vide infra), where only the stabilizing (nucleus-electron) and destabilizing (electron-electron) classical interactions are taken into account.

The TF theory gives a reasonable description of the charge density for heavy atoms. In fact, it can be demonstrated [Lieb & Simon, 1973] that this theory is exactly valid in the limit of an atomic number Z → ∞. Nevertheless, it fails if applied to molecular systems, because it is unable to predict the existence of any chemical bonds: in the ambit of the TF theory, the minimum energy for an aggregate of atoms is always given by nuclei at infinite distance [Teller, 1962].

1.3 The Hohemberg – Kohn Theorems

Hohenberg and Kohn (HK) [Hohenberg & Kohn, 1964] revolutionized the world of the theoretical chemistry demonstrating that the TF model had to be considered as an approximate form of an exact theory, now known as density functional theory (DFT). This is the consequence of the demonstration of the first and the second HK theorems. If we define an external potential $\upsilon(\boldsymbol{r}_i)$:

$$\upsilon\left(\boldsymbol{r}_i\right) = -\sum_p \frac{Z_p}{r_{ip}} \tag{1.3.1}$$

the first HK theorem justifies the use of $\rho(\boldsymbol{r})$ as basic variable. In fact, the first theorem establishes that the *external potential* $\upsilon(\boldsymbol{r})$ *is determined, apart from an additive constant, by the electron density* $\rho(\boldsymbol{r})$. Since the electron density integrates to the number of electrons N (see the Eq. (1.1.5)), it follows that the ground state wave function and all the electronic properties of the chemical system are univocally determined by the electron density. The relation between $\rho(\boldsymbol{r})$ and $\upsilon(\boldsymbol{r})$, together with the normalization condition in the Eq. (1.1.5), legitimate the use of ρ as basic variable, and allow to define the total energy in the Eq. (1.2.5) as a functional of the electron density ρ and explicating its dependence on $\upsilon(\boldsymbol{r})$:

$$E = E_\upsilon\left[\rho\right] = T\left[\rho\right] + V_{ee}\left[\rho\right] + V_{ne}\left[\rho\right] = F_{\mathrm{HK}}\left[\rho\right] + \int d\boldsymbol{r}\rho\left(\boldsymbol{r}\right)\upsilon\left(\boldsymbol{r}\right) \tag{1.3.2}$$

with

$$V_{ne}\left[\rho\right] = \int d\boldsymbol{r}\rho\left(\boldsymbol{r}\right)\upsilon\left(\boldsymbol{r}\right) \tag{1.3.3}$$

$$F_{\mathrm{HK}}\left[\rho\right] = T\left[\rho\right] + V_{ee}\left[\rho\right] \tag{1.3.4}$$

$$V_{ee}\left[\rho\right] = J\left[\rho\right] + E_{xc}\left[\rho\right] \tag{1.3.5}$$

where $F_{\mathrm{HK}}[\rho]$ is the HK functional, $J[\rho]$ represents the classic term of the Coulomb repulsion, while the major contribution to the $E_{\mathrm{xc}}[\rho]$ is due to the non-classical terms of exchange and correlation energies. It is noteworthy that $F_{\mathrm{HK}}[\rho]$ does not depend

upon the external potential, resulting an universal functional of $\rho(\mathbf{r})$.

The second theorem provides the variational principle for the energy. It establishes that, *given a trial electron density* $\tilde{\rho}(\boldsymbol{r})$*, with* $\tilde{\rho}(\boldsymbol{r}) \geq 0$*, and* $\int d\boldsymbol{r}\tilde{\rho}(\boldsymbol{r}) = N$

$$E_0 \leq E_\upsilon[\tilde{\rho}] \tag{1.3.6}$$

where $E_\upsilon[\tilde{\rho}]$ is the energy functional obtained from Eq. (1.3.2) with $\rho = \tilde{\rho}(\boldsymbol{r})$ while E_0 is the exact ground-state energy. The first HK theorem asserts that $\tilde{\rho}(\boldsymbol{r})$ determines its own external potential $\upsilon(\boldsymbol{r})$ and its wave function $\tilde{\Psi}$, which can be used as a trial function for the minimization problem:

$$\langle\tilde{\Psi}|\hat{H}|\tilde{\Psi}\rangle = F_{\mathrm{HK}}[\tilde{\rho}] + \int d\boldsymbol{r}\tilde{\rho}(\boldsymbol{r})\upsilon(\boldsymbol{r}) = E[\tilde{\rho}] \geq E[\rho] = \langle\Psi|\hat{H}|\Psi\rangle \tag{1.3.7}$$

The validity of the HK theorems is limited by the fact that F_{HK} is defined only for those trial ρ that are υ-representable, where a υ-representable ρ is an electron density associated with an antisymmetric ground state wave function of an Hamiltonian of the form (1.1.7) with a local external potential $\upsilon(\boldsymbol{r})$. Actually, $F_{\mathrm{HK}}[\rho]$ is a universal functional of ρ in that the same value is delivered for a given trial υ-representable ρ no matter what external potential is considered [Levy, 1979]. A limitation of $F_{\mathrm{HK}}[\rho]$ is that it is undefined for any ρ that is not υ-representable, and thus the theorems cease to apply. However, HK pointed out that it has not been proved that an arbitrary density distribution containing an integral number of electrons can be realized by some external potential [Hohenberg & Kohn, 1964; Gunnarsson & Lundqvist, 1976], and thus $F_{\mathrm{HK}}[\rho]$ can be redefined for electrons densities ρ satisfying the weaker condition of *N*-representability. A density is *N*-representable if it may be obtained from some antisymmetric wave function [Coleman, 1963]. The conditions for an electron density ρ to satisfy the *N*-representability can be fulfilled by any reasonable density [Gilbert, 1975]:

$$\rho(\boldsymbol{r}) \geq 0 \tag{1.3.8a}$$

$$\int d\boldsymbol{r}\rho(\boldsymbol{r}) = N \tag{1. 3.8b}$$

$$\int d\boldsymbol{r}\left|\nabla\rho(\boldsymbol{r})^{\frac{1}{2}}\right|^2 < \infty \tag{1. 3.8c}$$

Despite the great importance of the two HK theorems for DFT, they do not provide any operative strategy for any application. Particularly, the second theorem is simply an existence theorem and does not give any information about the construction of the ground state energy functional. In fact, the kinetic energy (T) and the electron-electron interaction (V_{ee}) functionals in Eq. (1.3.2), i.e., the universal functional F_{HK} in the Eq. (1.3.4), are still unknown and the existence of an exact theory justifies the research of new functionals that, even though approximate, can be more and more accurate. The reader interest to a quite detailed, but certainly incomplete, description of DFT historical developments may refer to the following reviews and books [Callaway et al., 1984; Becke, 1988c; Parr et al., 1989; Ziegler, 1991; Koch et al., 2001; Fiolhais C. 2003, Tsuneda, 2014].

1.4 The Kohn – Sham Equations

In 1965 Kohn and Sham (KS) proposed [Kohn & Sham, 1965] the most successful approach to treat indirectly the kinetic energy functional $T[\rho]$, making DFT a powerful method for rigorous calculations. KS proposed to introduce the orbitals into the problem in such a way that it could be possible to calculate the kinetic energy with a good approximation. The exact expression for the kinetic energy of the ground state can be expressed as [Parr & Yang, 1989]:

$$T\left[\rho\right] = -\frac{1}{2}\sum_{i=1}^{N} n_i \left\langle \psi_i \middle| \nabla^2 \middle| \psi_i \right\rangle \tag{1.4.1}$$

where ψ_i are the spin orbitals and n_i are their occupation numbers. The Pauli exclusion principle [Pauli, 1925] implies that $0 \leq n_i \leq 1$; furthermore, the first HK theorem ensures that the kinetic energy is a functional of the total charge density [Hohenberg & Kohn, 1964]. Any non-negative, continuous and normalized electron density ρ is N-representable and can be decomposed in [Gilbert, 1975]:

$$\rho\left(\boldsymbol{r}\right) = \sum_{i=1}^{N} n_i \sum_{s} \left|\psi_i\left(\boldsymbol{r}, s\right)\right|^2 \tag{1.4.2}$$

where $\psi_i(\boldsymbol{r}, s)$ represents a spin orbital with spatial coordinates $\boldsymbol{r}$ and spin coordinates s. Nevertheless, given an electron density, there is not a unique decomposition in terms of spin orbitals. Kohn and Sham started from considering the simplest expression for T and ρ:

$$T_S = -\frac{1}{2}\sum_{i=1}^{N} \left\langle \psi_i \middle| \nabla^2 \middle| \psi_i \right\rangle \tag{1.4.3}$$

and

$$\rho\left(\boldsymbol{r}\right) = \sum_{i=1}^{N} \sum_{s} \left|\psi_i\left(\boldsymbol{r}, s\right)\right|^2 \tag{1.4.4}$$

i.e., $n_i = 1$ for N orbitals, otherwise $n_i = 0$. The problem is to obtain an unique orbital decomposition providing one value of $T_S[\rho]$. The simplified representation of the electron density and of the kinetic energy proposed by KS correspond to a reference system of non-interacting electrons in absence of any electron-electron repulsion, and for which its ground state electron density is exactly $\rho(\boldsymbol{r})$. In analogy with the definition of the universal functional $F_{HK}[\rho]$, KS defined a system composed by non-interacting particles, with ground-state density $\rho(\boldsymbol{r})$, and Hamiltonian

$$\hat{H}_S = -\frac{1}{2}\sum_{i=1}^{N}\nabla_i^2 + \sum_{i=1}^{N}\upsilon_S(\boldsymbol{r}) \tag{1.4.5}$$

excluding any repulsive term. The ground state of such a system is exactly described by a single Slater determinant multi-electron wave function

$$\Psi_S = \frac{1}{\sqrt{N!}}\det(\psi_1\psi_2...\psi_N) \tag{1.4.6}$$

where ψ_i are the first N eigenvectors of the one-electron Hamiltonian

$$\hat{h}_S\psi_i = \left[-\frac{1}{2}\nabla^2 + \upsilon_S(\boldsymbol{r})\right]\psi_i = \varepsilon_i\psi_i \tag{1.4.7}$$

The kinetic energy of the reference system is simply $T_S[\rho]$, given by the Eq. (1.4.8)

$$T_S[\rho] = \langle\Psi_S\left|\left[-\frac{1}{2}\sum_{i=1}^{N}\nabla_i^2\right]\right|\Psi_S\rangle = -\frac{1}{2}\sum_{i=1}^{N}\langle\psi_i|\nabla^2|\psi_i\rangle \tag{1.4.8}$$

and the electron density is decomposed according to (1.4.4). Even though T_S can be defined univocally for any density, it is still not an exact kinetic energy functional, and the difference between the exact kinetic energy functional $T[\rho]$ and $T_S[\rho]$ lies in its exchange-correlation part. The success of the KS method lies in the fact that $T_S[\rho]$, which can be evaluated through the equation (1.4.8), is exactly the kinetic energy used

to determine the ground-state energy. This result can be obtained by writing

$$F_S[\rho] = T_S[\rho] + J[\rho] + E_{xc}[\rho] \tag{1.4.9}$$

$$J[\rho] = \frac{1}{2}\iint d\boldsymbol{r}\, d\boldsymbol{r}' \frac{\rho(\boldsymbol{r})\rho(\boldsymbol{r}')}{|\boldsymbol{r}-\boldsymbol{r}'|} \tag{1.4.10}$$

$$E_{xc}[\rho] \equiv T[\rho] - T_S[\rho] + V_{ee}[\rho] - J[\rho] \tag{1.4.11}$$

where $E_{xc}[\rho]$ is the exchange-correlation energy, and it includes the difference between $T[\rho]$ and $T_S[\rho]$, usually a small quantity, and $Vee[\rho]$ non-classical contributions. The KS iterative procedure operates as follows: defined an external potential $\upsilon(\boldsymbol{r})$, the orbitals are obtained by solving the N one-electron equations:

$$\left[-\frac{1}{2}\nabla^2 + \upsilon(\boldsymbol{r}) + \int d\boldsymbol{r}\frac{\rho(\boldsymbol{r}')}{|\boldsymbol{r}-\boldsymbol{r}'|} + \upsilon_{xc}(\boldsymbol{r})\right]\psi_i = \varepsilon_i\psi_i \tag{1.4.12}$$

where the exchange-correlation potential $\upsilon_{xc}(\boldsymbol{r})$ is defined as:

$$\upsilon_{xc}(\boldsymbol{r}) = \frac{\delta E_{xc}[\rho]}{\delta\rho(\boldsymbol{r})} \tag{1.4.13}$$

The electron density ρ is computed through the equation (1.4.4) and the new density ρ is substituted in equation (1.4.12) where is used to compute the new orbitals ψ_i. The iterative cycle is repeated until the self-consistency is reached.
The total energy for the system at each step is:

$$E = -\frac{1}{2}\sum_{i=1}^{N}\langle\psi_i|\nabla^2|\psi_i\rangle + J[\rho] + E_{xc}[\rho] + \int d\boldsymbol{r}\rho(\boldsymbol{r})\upsilon_{ex}(\boldsymbol{r}) \tag{1.4.13}$$

1.5 The Electron Exchange and Correlation

In order to evaluate the total energy (1.4.13) of a chemical system, thanks to KS a procedure to compute the kinetic energy has been developed. As far as the electron-electron repulsion V_{ee} in (1.3.5), it has been already pointed out that it is sum of two contributions, $J[\rho]$ and $E_{xc}[\rho]$. The exact form of the exchange-correlation functional $E_{xc}[\rho]$ is still unknown, and thus several approximated forms have been built up to gain fairly accurate results on many chemical systems. If we define the *exchange-correlation* hole as:

$$h_{xc}\left(\boldsymbol{r}_1,\boldsymbol{r}_2\right)=\frac{\rho_2\left(\boldsymbol{r}_1,\boldsymbol{r}_2\right)}{\rho\left(\boldsymbol{r}_1\right)}-\rho\left(\boldsymbol{r}_2\right) \tag{1.5.1}$$

then, the interelectronic repulsion V_{ee} can be rewritten as:

$$V_{ee}=\frac{1}{2}\iint d\boldsymbol{r}_1 d\boldsymbol{r}_2\frac{\rho\left(\boldsymbol{r}_1\right)\rho\left(\boldsymbol{r}_2\right)}{\left|r_1-r_2\right|}+\frac{1}{2}\iint d\boldsymbol{r}_1 d\boldsymbol{r}_2\frac{\rho\left(\boldsymbol{r}_1\right)}{\left|r_1-r_2\right|}h_{xc}\left(\boldsymbol{r}_1,\boldsymbol{r}_2\right)=J\left[\rho\right]+E_{xc} \tag{1.5.2}$$

The exchange and correlation tend to keep electrons apart, so the exchange and correlation contributions can be described in terms of a hole surrounding each electron and keeping other electrons from approaching it. The exchange-correlation hole can be interpreted in relation to the combined probability to find an electron at point $\boldsymbol{r}_1$ given the existence of another electron at point $\boldsymbol{r}_2$. The better the h_{xc} is approximated, the better is the accuracy reached by the resulting functional $E_{xc}[\rho]$. The accuracy of DFT calculations largely depends upon the quality of the approximations adopted for $\upsilon_{ex}(\boldsymbol{r})$ in Eq. (1.4.13), and for the corresponding $E_{xc}[\rho]$ in Eq. (1.3.5). It is noteworthy that the HK theorems are valid only with the exact exchange-correlation functional, whereas they are not for the approximated forms. Thus, practical approaches to DFT are no longer variational. Common approximated exchange-correlation functionals can be divided in four main groups, each of them related to different levels of approximation. The simplest approximation is the local density approximation (LDA) and the exchange-correlation functionals belonging to these groups depend only on the local value of the electron density $\rho(\boldsymbol{r})$:

$$E_{xc}^{LDA} = \int d\boldsymbol{r}\rho(\boldsymbol{r})\varepsilon_{xc}(\rho) \tag{1.5.3}$$

where ε_{xc} is the exchange-correlation energy per electron and it is given by the uniform electron gas formula in the ambit of the TF theory. The exchange-correlation energy can be split in two terms:

$$E_{xc} = E_x + E_c \tag{1.5.4}$$

where the exchange energy contribution E_x is defined as [Dirac, 1930]:

$$\varepsilon_x^{LDA}[\rho] = -\frac{3}{4}\left(\frac{3}{\pi}\right)^{\frac{1}{3}}\int d\boldsymbol{r}\rho(\boldsymbol{r})^{\frac{4}{3}} \tag{1.5.5}$$

while the correlation term E_c is obtained analytically by interpolating the quantum Monte Carlo results [Ceperley & Alder, 1980; Vosko et al., 1980; Perdew & Zunger, 1981; Perdew & Wang, 1992] or by adopting other approaches [Wigner, 1934; Cole & Perdew, 1982; Lee et al., 1988]. Despite the rather rough approximation, the LDA works surprisingly fine for describing many real chemical systems. Later on, more complex schemes aimed to overcome the LDA limits have been proposed to reach a better accuracy of the method. In this regard, it is noteworthy that the main source of error in the LDA based $E_{xc}[\rho]$ lies in the exchange component and many contributions have been then focused on the research of suitable corrections of E_x [Langreth et al., 1983; Becke, 1983; Perdew, 1985; Perdew et al., 1986; Becke, 1986; De Pristo et al., 1987; Becke, 1988a-c; Tschinke et al., 1989; Perdew et al., 1989]. Thus, to go beyond LDA the inhomogeneity of the electron density must be considered. The exchange energy is calculated by adding to the LDA based $E_{xc}[\rho]$ the non-local correction term (E_x^{NL}), which depends upon the gradient of the electron density, in order to take somehow into account the non-uniformity of the density in a real system. This class of functionals are called Generalized Gradient Approximation (GGA) functionals. The exchange functional has the following general form:

$$E_x^{GGA} = E_x^{LDA} - \int d\boldsymbol{r} g(\chi)\left[\rho(\boldsymbol{r})\right]^{\frac{4}{3}} \tag{1.5.6}$$

where $g(\chi)$ is a function of the parameter

$$\chi = \frac{\left|\nabla\rho(\boldsymbol{r})\right|}{\left[\rho(\boldsymbol{r})\right]^{\frac{4}{3}}} \tag{1.5.7}$$

and the form of $g(\chi)$ depends on the particular GGA functional under consideration. Before going on, it has to be noticed that most GGA exchange functionals have unique behaviors only for large χ [Tsuneda et al., 1999; Tsuneda et al., 2001]. This is because small χ behaviors of functionals are restricted by the physical condition for slowly-varying density [Kleinman & Lee, 1988], although there is no definite conditions for rapidly-varying density [Tsuneda et al., 1999; Tsuneda & Hirao, 2000; Tsuneda et al., 2001]. Hence, GGA exchange functionals are usually characterized by the behaviors for large χ (*i.e.*, low-density-high-gradient) density. Great attention has been devoted to find the gradient correction able to provide values of the exchange energy closer to the exact quantity, and in literature many non-local corrections are available [Becke, 1983; Perdew, 1985; Perdew, 1986; Perdew & Wang, 1986; Becke, 1986; Becke, 1988a-c; Perdew & Wang, 1989]. Another family of exchange-correlation functions is that of the so-called meta-GGA functionals, whose formula includes a contribution related to the positive kinetic energy density of the occupied orbital KS orbitals [Tao et al., 2003]. Moreover, two other classes of exchange-correlation functionals with approximations more complicated and more accurate can be considered: in hyper-GGA functionals the exact exchange energy density is added [Perdew et al., 2008], and generalized random phase approximation functionals consider the unoccupied orbitals [Constantin et al., 2008]. It can be observed that increasing the complexity of the approximations typically more accurate results can be achieved with computation costs increasing modestly from the LDA to the meta-GGA and much more steeply after that [Perdew et al. 2009]. Furthermore, another important class of exchange-correlation functionals uses the KS orbitals of the chemical system to compute the exchange through its exact formula from the Hartree-Fock theory, and for this reason these are called hybrid functionals [Ernzerhof & Scuseria, 1999; Adamo & Barone, 1999; Stephens et al. 1994].

1.6 The Long-range Correction

Long-range (LR) correction refers to the correction of exchange functionals for LR electron–electron exchange interactions, which are poorly included in conventional exchange functionals. These usually depend only on the electron distribution; thus, they essentially contain no explicit electron–electron interactions and it sounds then reasonable to suppose that exchange functionals always require a LR correction. Incidentally, LR exchange interactions are naturally present in the Hartree–Fock exchange integral, which is an explicit two electron coordinate integral. For the LDA exchange functional [Dirac, 1930], Savin suggested the formulation of a LR correction scheme [Savin, 1996], which makes it applicable in quantum chemistry calculations. In this scheme, the two-electron operator, $(r_{12})^{-1}$, is factorized by the standard error function[3] as

$$\frac{1}{r_{12}} = \frac{1 - erf\left(\mu r_{12}\right)}{r_{12}} + \frac{erf\left(\mu r_{12}\right)}{r_{12}} \qquad (1.6.1)$$

In other words, $(r_{12})^{-1}$ is separated into the short-range (SR) and LR parts by the standard error function with μ representing a parameter, which determines the ratio of these parts. Even without entering into details, it of some relevance to outline that the LR correction has allowed the solution of a large variety of problems, the most relevant of which certainly are: i) the evaluation of van der Waals (vdW) binding energies (see the next section); ii) the modeling of electronic excitation spectra; iii) the optical response properties and orbital energies.

[3] The error function, often called Gauss error function, is a special function of sigmoid shape, which occurs in probability, statistics and partial differential equations describing diffusion. It is defined as $erf\left(x\right) = \frac{2}{\sqrt{\pi}}\int_0^x e^{-u^2}du = 1 - \frac{2}{\sqrt{\pi}}\int_x^\infty e^{-u^2}du$; for this definition $erf(0) = 0$; $erf(\infty) = 1$, $erf(-x) = -erf(x)$ (the interested reader may refer to Riley et al., 2006)

1.7 The van der Waals Corrections

A quite large number of physical phenomena that are responsible for attraction and repulsion between molecules can be identified. All of the important ones arise ultimately from the electrostatic interaction between the particles comprising the two molecules. They can be separated into two main types: ii) LR, where the energy of interaction behaves as some inverse power of the distance between the interacting molecules, and ii) SR, where the energy decreases in magnitude exponentially with distance. Such an apparently arbitrary distinction has a clear foundation in theory. LR effects are of three kinds: electrostatic, induction and dispersion. Electrostatic effects are the simplest one to be understood. In general terms, they arise from the straightforward classical interaction between the static charge distributions of the two interacting molecules; they are strictly pairwise additive and may be either attractive or repulsive. Induction effects arise from the distortion of a particular molecule in the electric field of all its neighbors, and they are always attractive. Moreover, because the fields of several neighboring molecules may reinforce each other or cancel out, induction effects are strongly non-additive. As far as dispersion effects are concerned, they cannot easily understood in classical terms, in fact they arise because molecular charge distributions are constantly fluctuating. The electron motions in two interacting molecules become correlated in such a way that lower-energy configurations are favored and higher-energy ones disfavored. The average effect is a lowering of the energy, and since the correlation effect becomes stronger as the molecules approach each other, the result is an attraction. A. J. Stone [Stone, 2013], in his inspiring book devoted to the intermolecular forces, provides the classification of the contributions to the energy of interaction between molecules (see Table 1.1).

Even though systematically neglected in the development of correlation functionals, “the vdW interaction is one of the most significant types of electron correlations” [Tsuneda, 2014]. vdW interactions, seminally reviewed by F. London and H. Margenau in the late 1937 and 1939, respectively [London, 1937; Margenau, 1939], collectively includes dipole-dipole, dipole-induced dipole and dispersion interactions [Israelachvili, 1992].

Table 1.1.1 Contributions to the energy of different interactions between molecules

Contribution	Additive?	Sign	Comment
LR ($E \sim R^{-n}$)			
Electrostatic	Yes	±	Strong orientation dependence
Induction	No	–	
Dispersion	Approx.	–	Always present
Resonance	No	±	Degenerate states only
Magnetic	Yes	±	Very small
SR ($E \sim e^{-aR}$)			
Exchange-repulsion	Approx.	+	Dominates at very short range
Exchange-induction	Approx.	–	
Exchange-dispersion	Approx.	–	
Charge transfer	No	–	Donor-acceptor interaction

As already mentioned, the dipole-dipole interaction is the electrostatic interaction between permanent dipoles in polar systems, while dipole-induced dipole interaction is the interaction between polar and nonpolar systems. As far as the universal dispersion interaction, which takes place even between bodies with neither charge nor multipole moment, it may be classically estimated through the London formula (1.7.1), firstly proposed at the beginning of the last century [London, 1930].

$$V_d^L(r) = -\frac{3}{2}\frac{\alpha_A \alpha_B}{(4\pi\varepsilon_0)^2 r_{AB}^6}\frac{I_A I_B}{I_A + I_B} \qquad (1.7.1)$$

where I_X is the ionization potential of the species X, r_{AB} is the distance between A and B and α_X is the X polarizaility. As such, the dispersion interaction may be interpreted as the interaction between an instantaneous dipole moment, generated by a fluctuation of the electron distribution, and an induced dipole moment, due to the electric field formed by the instantaneous dipole moment. In other words, two spatially separated electron distributions fluctuate around their equilibrium distributions by electron correlation to produce interactions between the two bodies. As such, the origin of the dispersion interaction is manifest: a pure electron correlation between two bodies,

which cannot be incorporated in the one-body mean-field approximation; even more specifically, a LR correlation explicitly acting between distant electrons. Even though the dispersion interaction should be included in correlation functionals, it has usually not been taken into consideration. Conventional GGA correlation functionals have been developed by density gradient corrections for the LDA correlation functional or by incorporating the dynamical correlation coming from the correlation cusp. Since these functionals include only the SR correlation resulting from correlation holes, the LR correlation, including dispersion interactions, is neglected. It is then not particularly surprising that KS calculations exploiting GGA correlation functionals, which neglect dispersion interactions have almost always failed even in a qualitative estimate of van der Waals bonds. It is, therefore, reasonable to consider that dispersion interactions should be explicitly supplemented in conventional correlation functionals. So far, various types of dispersion corrections have been suggested. These dispersion corrections are generally classified into five types: i) classical dispersion corrections; ii) combinations with perturbation theories; iii) linear-response theories; iv) van der Waals (dispersion) functionals; v) semiempirical dispersion-corrected functionals. In addition to these dispersion corrections, LR exchange interactions and correlation functionals are also significant in calculating van der Waals bonds [Kristyan et al, 1994; Tsuneda, 2014].

1.8 The Perturbation Theory of Dispersion Forces

Dispersion represents the main interaction between non-polar molecules at large distance; i.e., when the superposition of the electron clouds becomes negligible. Let us consider two neutral and non-polar molecules *A* and *B*, whose wave functions Ψ_A and Ψ_B are non-zero in different regions of the space. As long as Ψ_A and Ψ_B do not overlap, calculations can be done without requiring antisymmetrization of the total wave function. This allows us to identify a set of N_A electrons belonging to *A* and for which a Hamiltonian $\hat{H}_A$ can be defined (analogous considerations hold for *B*). The unperturbed Hamiltonian $\hat{H}^0$ for the coupled system will then be:

$$\hat{H}^0 = \hat{H}_A + \hat{H}_B \tag{1.8.1}$$

whose eigenfunction, according to the "physical meaning" associated to Ψ_A and Ψ_B, will be the simple products $\Psi_i^A \Psi_j^B$, hereafter simplified as $\left|i,j\right\rangle$.

$$\hat{H}^0 \left|i,j\right\rangle = \left(\hat{H}_A + \hat{H}_B\right)\left|i,j\right\rangle = \left(E_i^A + E_j^B\right)\left|i,j\right\rangle = E_{ij}^0 \left|i,j\right\rangle \tag{1.8.2}$$

Incidentally, indexes *i* and *j* of the Eq. (1.8.2) label specific electronic states of *A* and *B*, respectively. As usual, the electrostatic interaction between molecules is treated as a perturbation

$$\hat{H}' = \sum_{a\in A}\sum_{b\in B}\frac{1}{r_{ab}} \tag{1.8.3}$$

The application of the ordinary Rayleigh-Schrödinger perturbation theory [Rayleigh, 1894; Schrödinger, 1926d] allows us to write the total energy E_{00} for the ground state $\left|0,0\right\rangle$ of the coupled system as

$$E_{00} = E_{00}^0 + E_{00}' + E_{00}'' + \ldots \tag{1.8.4}$$

where

$$E_{00} = E_{00}^{A} + E_{00}^{B} \tag{1.8.5}$$

$$E'_{00} = \langle 00 | \hat{H}' | 00 \rangle \tag{1.8.6}$$

$$E''_{00} = -{\sum_{ij}}' \frac{\langle 00 | \hat{H}' | ij \rangle \langle ij | \hat{H}' | 00 \rangle}{E_{ij}^{0} - E_{00}^{0}} \tag{1.8.7}$$

The prime on summation implies that i and j cannot be simultaneously zero.

The first order correction (1.8.6) simply accounts for the electrostatic interaction between the charge density of the two molecules

$$E'_{00} = \int d\boldsymbol{r}\, d\boldsymbol{r}' \frac{\rho^{A}(\boldsymbol{r}) \rho^{B}(\boldsymbol{r}')}{|\boldsymbol{r} - \boldsymbol{r}'|} \tag{1.8.8}$$

while the second order correction (1.8.7) involves both induction and dispersion. To realize that, we may separate E''_{00} in three parts (Stone, 2013) by considering separately the terms in the sum for which molecule A is excited but B is in its ground state, the terms for which molecule B is excited but A is in its ground state, and the terms where both molecules are excited (the only term excluded in the sum is the one in which both molecules are in their ground state).

$$E''_{00} = U_{ind}^{A} + U_{ind}^{B} + U_{disp} \tag{1.8.9}$$

with

$$U_{ind}^{A} = -\sum_{i \neq 0} \frac{\langle 00 | \hat{H}' | i0 \rangle \langle i0 | \hat{H}' | 00 \rangle}{E_{i}^{A} - E_{0}^{A}} \tag{1.8.10}$$

$$U_{ind}^{B} = -\sum_{j \neq 0} \frac{\langle 00 | \hat{H}' | 0j \rangle \langle 0j | \hat{H}' | 00 \rangle}{E_{j}^{B} - E_{0}^{B}} \tag{1.8.11}$$

$$U_{disp} = -\sum_{i,j \neq 0} \frac{\langle 00 | \hat{H}' | ij \rangle \langle ij | \hat{H}' | 00 \rangle}{E_{i}^{A} + E_{j}^{B} - E_{0}^{A} - E_{0}^{B}} \tag{1.8.12}$$

Equations (1.8.10), (1.8.11), and (1.8.12) describe the induction energy of molecule *A*, the induction energy of molecule *B*, and the dispersion energy, respectively. The equation (1.8.12) may be worked out by exploiting the multipole expression for $\hat{H}'$ (Stone, 2013)

$$\hat{H}' = -\hat{T}_{\alpha\beta}\hat{\mu}^A_\alpha\hat{\mu}^B_\beta - \frac{1}{3}\hat{T}_{\alpha\beta\gamma}\left(\hat{\mu}^A_\alpha\Theta^B_{\beta\gamma} - \Theta^A_{\alpha\beta}\hat{\mu}^B_\gamma\right) - \hat{T}_{\alpha\beta\gamma\delta}\left(\frac{1}{15}\hat{\mu}^A_\alpha\Omega^B_{\beta\gamma\delta} - \frac{1}{9}\Theta^A_{\alpha\beta}\Theta^B_{\gamma\delta} + \frac{1}{15}\Omega^A_{\alpha\beta\gamma}\hat{\mu}^B_\delta\right) + \ldots \quad (1.8.13)^4$$

where $\hat{\mu}^A_\alpha$, $\Theta^A_{\alpha\beta}$ and $\Omega^A_{\alpha\beta\gamma}$ are the matrix elements of the dipole, quadrupole and octupole moment operators, respectively, acting on the molecule *A*. The equation (1.8.13) takes into account dipole-dipole, dipole-quadrupole, dipole-octupole and quadrupole-quadrupole interactions. All the terms of the multipolar expansion (1.8.13) depending on net charges have been omitted for we have to deal with non-charged molecules. Now, keeping in mind that $\hat{H}'$ is leaded by dipole-dipole interactions, we may consider only the first term in the RHS of the equation (1.8.13) to obtain

$$U_{disp} = -\sum_{i,j\neq 0}\frac{\left\langle 00\left|\hat{\mu}^A_\alpha\hat{T}_{\alpha\beta}\hat{\mu}^B_\beta\right|ij\right\rangle\left\langle ij\left|\hat{\mu}^A_\gamma\hat{T}_{\gamma\delta}\hat{\mu}^B_\delta\right|00\right\rangle}{E^A_i + E^B_j - E^A_0 - E^B_0} = -\hat{T}_{\alpha\beta}\hat{T}_{\gamma\delta}\sum_{i,j\neq 0}\frac{\left\langle 0^A\left|\hat{\mu}^A_\alpha\right|i^A\right\rangle\left\langle i^A\left|\hat{\mu}^A_\gamma\right|0^A\right\rangle\left\langle 0^B\left|\hat{\mu}^A_\beta\right|j^B\right\rangle\left\langle j^B\left|\hat{\mu}^A_\delta\right|0^B\right\rangle}{W^A_{i0} + W^B_{j0}} \quad (1.8.14)$$

where $W^A_{i0} = E^A_i - E^A_0$ and we exploited the evidence that $\hat{\mu}^A$ acts only on the electronic coordinate of *A*. Now, the matrix elements are factorized into terms referring to *A* and terms referring to *B*, but the denominator is not. To handle it, London [London, 1930] used the average-energy approximation [Unsöld, 1927].

[4] In atomic units, $\hat{T} = \frac{1}{R}$ and $\hat{T}_{\alpha\beta\ldots\nu} = \nabla_\alpha\nabla_\beta\ldots\nabla_\nu\frac{1}{R}$

$$U_{disp} = -\hat{T}_{\alpha\beta}\hat{T}_{\gamma\delta}\sum_{i,j\neq 0}\frac{W_{i0}^{A}W_{j0}^{B}}{W_{i0}^{A}+W_{j0}^{B}} \times\frac{\left\langle 0^{A}\left|\hat{\mu}_{\alpha}^{A}\right|i^{A}\right\rangle\left\langle i^{A}\left|\hat{\mu}_{\gamma}^{A}\right|0^{A}\right\rangle}{W_{i0}^{A}}\frac{\left\langle 0^{B}\left|\hat{\mu}_{\beta}^{A}\right|j^{B}\right\rangle\left\langle j^{B}\left|\hat{\mu}_{\delta}^{A}\right|0^{B}\right\rangle}{W_{j0}^{B}} \tag{1.8.15}$$

$$\frac{W_{i0}^{A}W_{j0}^{B}}{W_{i0}^{A}+W_{j0}^{B}} \approx \frac{U_{A}U_{B}}{U_{A}+U_{B}}\left(1+\Delta_{ij}\right) \tag{1.8.16}$$

with

$$\Delta_{ij} = \frac{\frac{1}{U_{A}}-\frac{1}{W_{i0}^{A}}+\frac{1}{U_{B}}-\frac{1}{W_{j0}^{B}}}{\frac{1}{W_{i0}^{A}}-\frac{1}{W_{j0}^{B}}} \tag{1.8.17}$$

With a proper choice of U_A and U_B, Δ_{ij} becomes negligible for all i and j and U_{disp} reduces to

$$U_{disp} \approx -\frac{U_{A}U_{B}}{4\left(U_{A}+U_{B}\right)}\hat{T}_{\alpha\beta}\hat{T}_{\gamma\delta}\alpha_{\alpha\gamma}^{A}\alpha_{\beta\delta}^{B} \tag{1.8.18}$$

with

$$\alpha_{\alpha\beta} = \sum_{j\neq 0}\frac{\left\langle 0\left|\hat{\mu}_{\alpha}\right|j\right\rangle\left\langle j\left|\hat{\mu}_{\beta}\right|0\right\rangle+\left\langle 0\left|\hat{\mu}_{\beta}\right|j\right\rangle\left\langle j\left|\hat{\mu}_{\alpha}\right|0\right\rangle}{W_{j}-W_{0}} \tag{1.8.19}$$

corresponding to the matrix elements of the polarizability tensor. For atoms, where $\alpha_{\alpha\beta}$ reduces to $\bar{\alpha}\delta_{\alpha\beta}$ we obtain the London formula for the U_{disp}.

$$U_{disp} \approx -\frac{U_{A}U_{B}}{4\left(U_{A}+U_{B}\right)}\hat{T}_{\alpha\beta}\hat{T}_{\gamma\delta}\bar{\alpha}^{A}\bar{\alpha}^{B} = -\frac{3}{2}\frac{U_{A}U_{B}}{\left(U_{A}+U_{B}\right)}\frac{\bar{\alpha}^{A}\bar{\alpha}^{B}}{R^{6}} \tag{1.8.20a}$$

$$U_{disp} \approx -\frac{C_{6}}{R_{AB}^{6}} \tag{1.8.20b}$$

$$C_6 = \frac{3}{2}\frac{U_A U_B}{\left(U_A + U_B\right)}\bar{\alpha}^A\bar{\alpha}^B \qquad (1.8.20c)$$

It is noteworthy that U_{disp} is always negative, i.e. it gives raise to attractive interactions between molecules. Moreover, dispersion energy is pairwise additive; this means that the total dispersion energy of a system composed by two or more molecules is just the sum of the dispersion energy between each pair of components. For practical purposes, the evaluation of 1.8.20a requires suitable values of the average excitation energies U_A and U_B. It is common use to equals them to the ionization energies, thus obtaining a rough approximation of C_6. Alternatively, using the lowest excitation energies of *A* and *B*, the Eqs. (1.8.20) provides an upper bound to the magnitude of dispersion. Slater & Kirkwood [Slater & Kirkwood, 1931] proposed a formula, in which U_A is approximated as $\sqrt{N_A / \alpha^A}$ where N_A is an effective number of valence electrons for molecule *A*.

1.9 Dispersion Forces in DFT

Dispersion interactions arise from the correlated motion of electrons and their proper treatment involves electronic excited states of the interacting species. This might be worked out by exploiting post Hartree-Fock (post-HF) approaches such as the Møller-Plesset perturbation theory [Møller & Plesset, 1934] at the second (MP2) or higher orders (MP*n*) and coupled cluster approach [Szabo & Ostlund, 1996; Williams & Chabalowski, 2001], but the computational cost becomes readily unsustainable even for medium-size systems. Even though DFT allows to handle chemical systems consisting of several hundreds of atoms and, in principle, the exact density functional would be able to account for dispersion interactions, commonly exploited local (LDA) and semi-local (GGA) functionals describe badly the physics of this kind of dynamical correlation [Kristyan & Pulay, 1994]. Among the several attempts devoted to the inclusion of dispersion effects in DFT, few of them will be considered in the following.

Dion et al. [Dion et al., 2004] proposed a non-local density functional explicitly accounting for dispersion corrections by means a non-local energy term

$$E_C^{NL} = \frac{1}{2\pi}\int_0^{\infty} \mathrm{tr}\left[\ln\left(1 - V\tilde{\chi}\right) - \ln\varepsilon\right] du \qquad (1.9.1)$$

where $\tilde{\chi}$ is the density response to the electric potential (neglecting spectator excitations), V is the interelectronic Coulomb interaction and ϵ is the (approximated) dielectric function; moreover, the integration runs over the imaginary frequency u.

Grimme [Grimme, 2006a], by taking advantage of the results obtained by Görling & Levy [Görling & Levy, 1993; Görling & Levy, 1994], included dispersion in DFT by developing a so-called double-hybrid functional, containing some amount of correlation computed at the MP2 level

$$E_C^{\mathrm{MP2}} = \frac{1}{4}\sum_{ia}\sum_{jb} \frac{\left|\left\langle ia\left|r_{12}^{-1}\right|jb\right\rangle - \left\langle ib\left|r_{12}^{-1}\right|ja\right\rangle\right|^2}{\varepsilon_i + \varepsilon_j - \varepsilon_a - \varepsilon_b} \qquad (1.9.2)$$

It is of some relevance to note that E_C^{MP2} is obtained by using KS orbitals. Moreover, it has also to be emphasized that Truhlar and co-workers developed a suite of strongly parameterized hybrid meta-GGA functionals [Zhao & Truhlar, 2008], which has been shown to model with good accuracy non covalent interactions. Although these strategies allow to treat dispersion forces with adequate accuracy, their computational cost is rather high, in particular when applied to the modeling of extended system such as crystalline polymers, organic/inorganic frameworks and self-assembled monolayers, where plane-wave basis sets are commonly employed. Indeed, the efficiency of plane-wave algorithms drops dramatically when non-local potentials are involved. This problem has been overcome by adding a semiempirical correction to the exchange-correlation functional in the form of a pairwise summation over the *M* atoms contained in the system

$$E_{disp} = -\sum_{i>j}^{M} f_{damp}\left(r_{ij}\right)\frac{C_{6ij}}{r_{ij}^{6}} \tag{1.9.3}$$

where $f_{damp}(r_{ij})$ is the damping function

$$f_{damp}\left(r_{ij}\right) = \frac{s_6}{1+\exp\left[-d\left(\frac{r_{ij}}{r_0}-1\right)\right]} \tag{1.9.4}$$

whose role is the exclusion of dispersion interactions at short distance, between directly bonded atoms. This method is known as dispersion-corrected DFT (DFT-D). Incidentally, s_6 represents a global-scaling parameter, whose value depends on the exchange-correlation functional actually used, while C_{6ij} coefficients are obtained from tabulated values of atomic C_{6i} coefficients through a square root combination rule [$C_{6ij} = (C_{6i}C_{6j})^{1/2}$] and r_0 is the sum of atomic vdW radii (Pauling, 1960). Although similar correction schemes were applied earlier even to Hartree-Fock calculations [Hepburn et al., 1975], the approach developed by Grimme [Grimme, 2006a-b] is innovative since the C_6 coefficients and vdW radii are computed rather than fitted or taken from experiments, which in principle allows to provide dispersion

parameters for the whole periodic table and not only for few atoms as happens in several implementations. Dispersion coefficients of atomic species are computed as:

$$C_{6i} = 0.05 N_A I_i \alpha_i \qquad (1.9.5)$$

where N_A is an effective number of electrons assuming the values 2, 10, 18, 36 and 54 for elements belonging to rows 1 – 5 of the periodic table, I_i and α_i are the ionization potential and the static dipole polarizability computed by means of unrestricted DFT calculations carried out using the PBE0 density functional [Adamo & Barone] with a QZPV basis set. As far as vdW radii are concerned, they are derived from the radius of the 0.01 au contour of electron density of the atom in their ground state, computed at the HF level of theory using a TZV basis set, scaled by a factor 1.1.

DFT-D is computationally cheap, it gives good results for a broad range of compounds [Grimme, 2006], and it may be used in conjunction with diverse Kohn-Sham energy functionals; last but not least, its accuracy may be further improved by refining ad-hoc atomic C_6 parameters and vdW radii for the system under study. Energy and gradients are easier to implement than those of other methods and can be straightforwardly extended to the periodic case, where also the stress tensor can be obtained analitically. As a final considerations, it should be pointed out that an exact implementation of the Eq. (1.9.3) would require the use of Ewald summation [Ewald, 1921]; however, since the dispersion energy decays as r^{-6}, it is absolutely convergent in crystals and the real-space summation (1.9.3) works properly.

Chapter 2

The Plane Wave Pseudopotential Method

2.1 Plane-wave Basis Sets

In the previous chapter it has been demonstrated that certain observables of the many-body problem can be mapped into equivalent observables in an effective single-particle problem. However, there still remains the problem of how to tackle an infinite number of noninteracting electrons moving in the static potential of an infinite number of nuclei or ions. More specifically, when facing the electronic structure of condensed matter systems, one is investigating the behavior of a number of electrons in the order of ~ 10^{28} per mole of atoms. As such, two difficulties have to be overcome: a wave function must be calculated for each of the infinite number of electrons in the system, and, since each electronic wave function extends over the entire solid, the basis set required to expand each wave function is infinite.

Both problems may be worked out by performing calculations on periodic systems[5] and applying the Bloch's theorem [Bloch, 1928] to the electronic wave functions, which states that in a periodic solid each electronic wave function can be expressed as the product of a plane-wave part and a periodic-cell part [Ashcroft & Mermin, 1976; Kittel, 2005],

$$\psi_i(\boldsymbol{r}) = \exp\left[i\boldsymbol{k}\cdot\boldsymbol{r}\right] f_i(\boldsymbol{r}) \qquad (2.1.1)$$

[5] Many extended systems are periodic in structure; i.e., they correspond to one of the Bravais lattices [Bravais, 1850]. In these cases, an infinite periodic system may be and calculations may be limited to the electrons of the periodic cell.

where the plane-wave part has wave-vector $\boldsymbol{k}$, which is confined to the first Brillouin zone (BZ) [Brillouin, 1930]. As far as the cell-periodic part of the wave function is concerned, it has the same periodicity of the lattice; i.e.,

$$f_i\left(\boldsymbol{r}+\boldsymbol{R}\right)=f_i\left(\boldsymbol{r}\right) \tag{2.1.2}$$

where $\boldsymbol{R}$ is one of the lattice vectors. This leads us to choose a plane-wave basis set to describe the wavefunction within the periodic cell. The periodic part of the wavefunction can then be written as:

$$f_i\left(\boldsymbol{r}\right)=\sum_{\mathbf{G}} c_{i,\mathbf{G}} \times e^{\left[i\mathbf{G}\cdot\boldsymbol{r}\right]} \tag{2.1.3}$$

where we have plane-wave coefficients $c_{i,\mathbf{G}}$ and $\mathbf{G}$ are the reciprocal lattice vectors satisfying the relationship

$$\mathbf{G}\cdot\boldsymbol{R}=2\pi m \tag{2.1.4}$$

for all the $\boldsymbol{R}$ and m being an integer. If we combine Eqs (2.1.1) and (2.1.3) KS orbitals can therefore be written as an infinite sum of plane-waves:

$$\psi_i\left(\boldsymbol{r}\right)=\sum_{\mathbf{G}} c_{i,\mathbf{G}+\boldsymbol{k}} e^{\left[i(\mathbf{G}+\boldsymbol{k})\cdot\boldsymbol{r}\right]} \tag{2.1.5}$$

where $c_{i,\mathbf{G}+\boldsymbol{k}}$ are the plane-wave coefficients describing the wavefunction.

Electronic states are allowed only at a set of $\boldsymbol{k}$ points determined by the boundary conditions that apply to the bulk solid. The density of allowed $\boldsymbol{k}$ points is proportional to the volume of the solid. The infinite number of electrons in the solid are accounted for by an infinite number of $\boldsymbol{k}$ points, and only a finite number of electronic states are occupied at each $\boldsymbol{k}$ point. The Bloch theorem thus changes the problem of calculating an infinite number of electronic wave functions to one of calculating a finite number of electronic wave functions at an infinite number of $\boldsymbol{k}$

points. The occupied states at each $\boldsymbol{k}$ point contribute to the electronic potential in the bulk so that, in principle, an infinite number of calculations are needed to compute this potential. However, the electronic wave functions at $\boldsymbol{k}$ points that are very close together will be almost identical. Hence, it is possible to represent the electronic wave functions over a region of $\boldsymbol{k}$ space by the wave functions at a single $\boldsymbol{k}$ point. In this case the electronic states at only a finite number of $\boldsymbol{k}$ points are required to calculate the electronic potential and hence determine the tota1 energy of the solid. Incidentally, the symmetry of the lattice may be used to reduce the number of $\boldsymbol{k}$-points required. The BZ can be made irreducible by applying the point group symmetries of the lattice, leaving no $\boldsymbol{k}$-points related by symmetry.

Diverse methods have been devised for obtaining very accurate approximations to the electronic potential and the contribution to the total energy from a filled electronic band by calculating the electronic states at special sets of $\boldsymbol{k}$ points in the Brillouin zone (Chadi & Cohen, 1973; Joannopoulos & Cohen, 1973; Monkhorst & Pack, 1976; Evarestov & Smirnov, 1983). Using these methods, one can obtain an accurate approximation for the electronic potential and the total energy of an insulator or a semiconductor by calculating the electronic states at a very small number of $\boldsymbol{k}$ points. The electronic potential and total energy are more difficult to calculate if the system is metallic because a dense set of $\boldsymbol{k}$ points is required to define the Fermi surface precisely. The magnitude of any error in the total energy due to inadequacy of the $\boldsymbol{k}$-point sampling can always be reduced by using a denser set of $\boldsymbol{k}$ points. The computed total energy will converge as the density of $\boldsymbol{k}$ points increases, and the error due to the $\boldsymbol{k}$-point sampling then approaches zero. In principle, a converged electronic potential and total energy can always be obtained provided that the computational time is available to calculate the electronic wave functions at a sufficiently dense set of $\boldsymbol{k}$ points.

Bloch's theorem states that the electronic wave functions at each $\boldsymbol{k}$ point can be expanded in terms of a discrete plane-wave basis set. In principle, an infinite plane-wave basis set is required to expand the electronic wave functions. However, the coefficients $c_{i,\boldsymbol{k}+\boldsymbol{G}}$ for the plane-waves with small kinetic energy $(\hbar^2/2m)|\boldsymbol{k} + \mathbf{G}|^2$ are typically more important than those with large kinetic energy.[6] Thus the plane-

[6] This corresponds to a sphere in reciprocal space within which all the used $|\boldsymbol{k} + \mathbf{G}|$ vectors lie.

wave basis set can be truncated to include only plane-waves that have kinetic energies less than some particular cutoff energy. If a continuum of plane-wave basis states were required to expand each electronic wave function, the basis set would be infinitely large no matter how small the cutoff energy. Application of the Bloch theorem allows the electronic wave functions to be expanded in terms of a discrete set of plane-waves. Introduction of an energy cutoff to the discrete plane-wave basis set produces a finite basis set. The truncation of the plane-wave basis set at a finite cutoff energy will lead to an error in the computed total energy. However, it is possible to reduce the magnitude of the error by increasing the value of the cutoff energy. In principle, the cutoff energy should be increased until the calculated total energy has converged; nevertheless, it can be demonstrates that it is possible to perform calculations at lower cutoff energies.

One of the difficulties associated with the use of plane-wave basis sets is that the number of basis states changes discontinuously with the cutoff energy. In general these discontinuities will occur at different cutoffs for different $\boldsymbol{k}$ points in the $\boldsymbol{k}$-point set. In addition, at a fixed-energy cutoff, a change in the size or shape of the unit cell will cause discontinuation in the plane-wave basis set. This problem can be reduced by using denser $\boldsymbol{k}$-point sets, so that the weight attached to any particular plane-wave basis state is reduced. However, the problem is still present even with quite dense $\boldsymbol{k}$-point samplings. It can be handled by applying a correction factor which accounts approximately for the difference between the number of states in a basis set with infinitely large number of $\boldsymbol{k}$ points and the number of basis states actually used in the calculation (Francis & Payne, 1990).

The use of plane-waves as a basis set is advantageous in a number of ways. In terms of the accuracy required for the system in question, one can always improve the accuracy by increasing the plane-wave cutoff energy and therefore tending towards the complete basis set. Real space quantities, such as potentials, can be easily transformed to reciprocal space using standard numerical techniques, in order to obtain the plane-wave coefficients. Derivatives in real space become multiplications in reciprocal space, so quantities such as the kinetic energy of the KS orbitals can be easily evaluated. The use of plane-waves treats all regions of space equally, so can be applied generally, even for non-periodic systems, if an appropriate periodic supercell is used. We make use of this in our forthcoming investigation concerning the modeling of two surface supported supramolecular architectures (see below).

However, this includes regions of vacuum, so there is an added memory and computational cost in such cases. A plane-wave basis set also lends well to distribution of data and processing in a parallel computing environment. This allows larger and more complicated systems to be simulated with higher accuracy.

When plane-waves are used as a basis set for the electronic wave functions, the KS equations assume a particularly simple form. Substitution of Eq. (2.1.3) into (1.4.12) and integration over $\boldsymbol{r}$ gives the secular equation

$$\sum_{\mathbf{G}'}\left[\begin{array}{l}\frac{\hbar}{2m}\left|\mathbf{G}+\boldsymbol{k}\right|^2\delta_{\mathbf{G}\mathbf{G}'}+\upsilon\left(\mathbf{G}-\mathbf{G}'\right)\\+\upsilon_H\left(\mathbf{G}-\mathbf{G}'\right)+\upsilon_{xc}\left(\mathbf{G}-\mathbf{G}'\right)\end{array}\right]c_{i,\mathbf{G}'+\boldsymbol{k}}=\varepsilon_i c_{i,\mathbf{G}'+\boldsymbol{k}} \qquad (2.1.4)^7$$

In this form, the kinetic energy is diagonal, and the various potentials are described in terms of their Fourier transforms. Solution of the Eq. (2.1.4) proceeds by diagonalization of a Hamiltonian matrix whose matrix elements $H_{\boldsymbol{k}+\mathbf{G},\boldsymbol{k}+\mathbf{G}'}$ are given by the terms in the brackets above. The size of the matrix is determined by the choice of the cutoff energy $(\hbar^2/2m)|\boldsymbol{k}+\mathbf{G}_c|^2$, and will be intractably large for systems including both valence and core electrons. This is a severe problem, which can be overcome by use of the pseudopotential approximation. The interested reader may refer to "Electronic Structure: basic theory and practical methods" [Martin, 2004].

The Bloch theorem can be applied neither to a system that contains a single defect nor in the direction perpendicular to a crystal surface. A continuous plane-wave basis set would be required for the defect calculation, and, although the plane-wave basis set for the surface calculation would be discrete in the plane of the surface, it would be continuous in the direction perpendicular to the surface. Hence an infinite number of plane-wave basis states would be required for both of these calculations, no matter how small the cutoff energy chosen for the basis set. Calculations using plane-wave basis sets can only be performed on these systems if a periodic supercell is used. The supercell for a point-defect calculation is illustrated schematically in Figure 2.1.1. The supercell contains the defect surrounded by a sufficiently extended region of the crystal. Periodic boundary conditions are applied to the supercell so that

---

[7] $\upsilon_H(\boldsymbol{r})=\int d\boldsymbol{r}\,\frac{\rho(\boldsymbol{r}')}{|\boldsymbol{r}-\boldsymbol{r}'|}$

it is reproduced throughout space. The energy per unit cell of a crystal containing an array of defects is calculated, rather than the energy of a crystal containing a single defect.

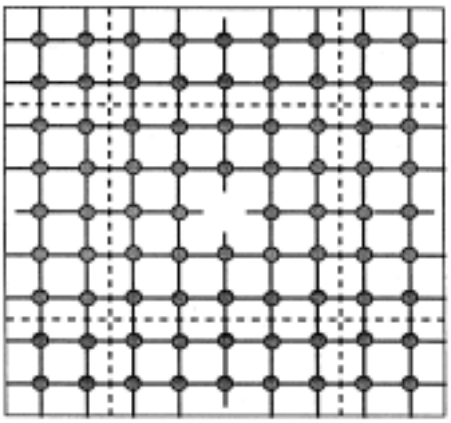

Figure 2.1.1 Schematic representation of a supercell geometry representative of a point defect (a vacancy) in the extended solid. The supercell is outlined by dashed lines.

Obviously, a key role is played by the supercell dimensions; i.e., it is of fundamental importance to include enough bulk solid in the supercell to prevent the defects in neighboring cells from interacting appreciably with each other. The independence of defects in neighboring cells can be checked by increasing the volume of the supercell until the computed defect energy has converged. It can then be assumed that defects in neighboring unit cells no longer interact. Analogous considerations hold for a surface, which may have periodicity in the plane of the surface itself, but it cannot in a direction perpendicular to the surface. The supercell for a surface calculation is depicted schematically in the left panel of Figure 2.1.2. The supercell includes a crystal slab and a vacuum region. The supercell is repeated over all space, so the total energy of an array of crystal slabs is calculated. To ensure that the results of the calculation accurately represent an isolated surface, the vacuum regions need to be wide enough so that faces of adjacent crystal slabs do not interact across the vacuum region, and the crystal slab must be thick enough so that the two surfaces of each crystal slab do not interact through the bulk crystal. Finally, even isolated molecules may be studied in this fashion, as illustrated in the right panel of Figure 2.1.2. Again, the supercell needs to be large enough so that the interactions between adjacent molecules are negligible.

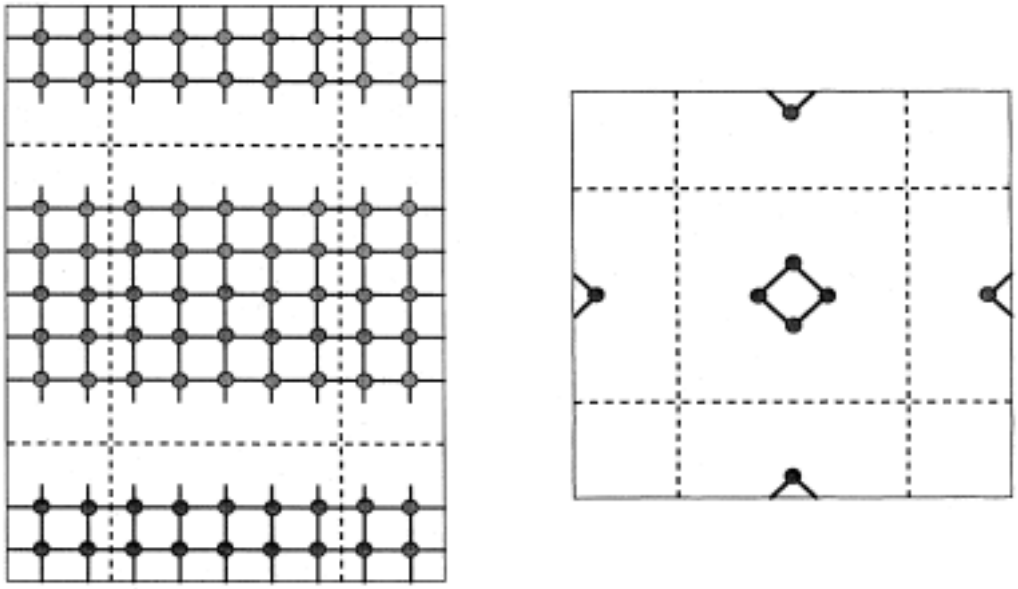

Figure 2.1.2 Schematic representation of a supercell geometry representative of: (left panel) a surface in the extended solid and (right panel) an isolated molecule. The supercell is outlined by dashed lines.

2.2 The Pseudopotential approximation

Although Bloch's theorem states that the electronic wave functions may be expanded by using a discrete set of plane-waves, a plane-wave basis set is usually very poorly suited to expanding electronic wave functions because a very large number of plane waves are needed to expand the tightly bound core orbitals and to follow the rapid oscillations of the wave functions of the valence electrons in the core region. An extremely large plane-wave basis set would be required to perform an all-electron calculation, and a huge amount of computational time would be required to calculate the electronic wave functions. The pseudopotential approximation (Phillips, 1958; Heine & Cohen, 1970; Yin & Cohen, 1982) allows the electronic wave functions to be expanded using a much smaller number of plane-wave basis states. It is well known that most physical properties of solids are dependent on the valence electrons to a much greater extent than on the core electrons. The pseudopotential approximation exploits this by removing the core electrons and by replacing them and the strong ionic potential by a weaker pseudopotential that acts on a set of pseudo wave functions rather than the true valence wave functions. An ionic potential, valence wave function and the corresponding pseudopotential and pseudo wave function are illustrated schematically in Figure 2.2.1.

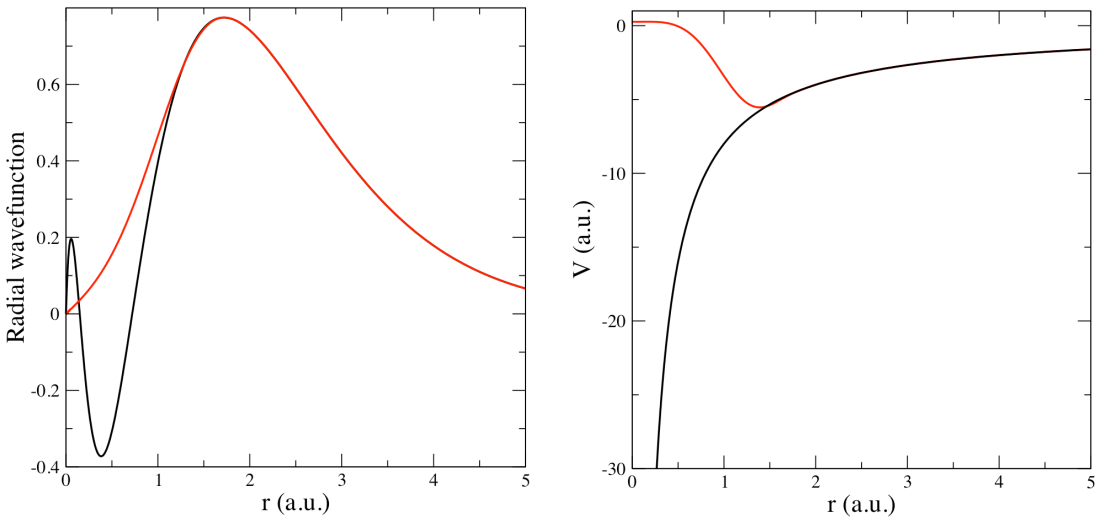

Figure 2.2.1 (left) The all-electron wavefuntion (black line) and the pseudowavefunction (red line) for the 3s orbital in Si. (right) The all-electrons potential (black line) and the pseudoppotential (red line) felt by the pseudised 3s orbital. The radius at which all-electron and pseudoelectron values match is designated r_C (not displayed in the Figure).

The valence wave functions oscillate rapidly in the region occupied by the core

electrons due to the strong ionic potential in this region. These oscillations maintain the orthogonality between the core wave functions and the valence wave functions, which is required by the exclusion principle. The pseudopotential is constructed, ideally, so that its scattering properties or phase shifts for the pseudo wave functions are identical to the scattering properties of the ion and the core electrons for the valence wave functions, but in such a way that the pseudo wave functions have no radial nodes in the core region. In the core region, the total phase shift produced by the ion and the core electrons will be greater by π, for each node that the valence functions had in the core region, than the phase shift produced by the ion and the valence electrons. Outside the core region the two potentials are identical, and the scattering from the two potentials is indistinguishable. The phase shift produced by the ion core is different for each angular momentum component of the valence wave function, and so the scattering from the pseudopotential must be angular momentum dependent. The most general form for a pseudopotential is

$$V_N^L = \sum_{\ell m} \left|\ell m\right\rangle V_\ell \left\langle \ell m\right| \qquad (2.2.1)$$

where $\left|\ell m\right\rangle$ are the spherical harmonics of degree ℓ and order m, while V_ℓ is the pseudopotential for the angular momentum having as quantum number ℓ. Acting on the electronic wave function with this operator decomposes the wave function into spherical harmonics, each of which is then multiplied by the relevant pseudopotential V_ℓ.

A pseudopotential that uses the same potential for all the angular momentum components of the wave function is called a local pseudopotential. A local pseudopotential is a function only of the distance from the nucleus. It is possible to produce arbitrary, predetermined phase shifts for each angular momentum state with a local potential, but there are limits to the amount that the phase shifts can be adjusted for the different angular momentum states, while maintaining the crucial smoothness and weakness of the pseudopotential. Without a smooth, weak pseudopotential it becomes difficult to expand the wave functions using a reasonable number of plane-wave basis states.

2.3 The Minimization of the Total Energy

The KS equations (Eq. 1.4.12) become a problem of matrix diagonalization when expressed in terms of plane waves. However, numerical algorithms for matrix diagonalization do not scale well with the size of the matrix in question. This both limits the number of plane waves and number of atoms in the periodic cell that can be practically used. Alternative methods involve direct minimization of the KS total energy functional. This is done through variation of the plane wave coefficients of the KS orbitals while ensuring that each band is orthogonal to the others. Among those methods one of the most efficient is the conjugate gradients technique [Polak, 1971]. This proceeds by taking an initial search direction to be that with the steepest gradient for the function and variable in question. That line is then followed to find the minimum. Subsequent search directions are then chosen such that they are independent of any previous minimization directions. This then guarantees the minimum will be found in the same number of steps as there are dimensions in the system. In practice, each band is treated one at a time to save memory costs in computation, made possible by keeping the bands orthogonal. The minimization procedure can be improved by using a preconditioning scheme [Teter et al., 1989; Gill et al., 1981]. This is because the plane waves with high kinetic energy dominate the search directions even though the corresponding coefficients in the wavefunction are small. Preconditioning is generally performed through multiplying the hamiltonian by a diagonal matrix consisting of the inverse kinetic energy operator for the high kinetic energy plane waves and a constant for the low kinetic energy plane waves. For the high kinetic energy plane waves, the energies will be dominated by the kinetic energy so any errors introduced by such an approximate preconditioning matrix will be small. In practice this allows convergence within tens of iterations for a basis set containing $\sim 10^6$ plane-waves.

Chapter 3

Case Study n° 1

3.1 Surface-confined 2D polymerization of the 1,2-bis(4-bromophenyl) ethyne on Ag(110).

Introduction: Acetylenic monodisperse oligomers [Martin & Diederich, 1999] and polydisperse high molecular weight polymers [Bunz, 2000; Bunz, 2005; Advances in Polymer Science, 2005; Ortiz et al., 2017] have been the focus of intense research in the last twenty years. Oligo- and poly(aryleneethynylenes) (OAE, PAE) constitute a broad class of such materials, characterized by a repeat unit containing an aryl group linked to an alkyne spacer (Scheme 1), which is responsible for a high degree of structural rigidity and a highly π-conjugated electronic structure of the resulting oligomeric/polymeric chains. The latter can be modulated by the proper choice and functionalization of the arylene units, the simplest being phenylene (leading to poly(phenyleneethynylene), PPE). As a result, an impressive array of applications has been envisaged for PAEs, which comprise optoelectronics [Montali et al., 1998] and chemical sensing [Swager, 2008] (due to their remarkable photoluminescence quantum yield, thermo- and photostability), light polarization [Weder et al., 1998], organic photovoltaics [Kastner et al., 2012] and – in highly branched 2D and 3D morphologies – porous materials for gas adsorption/capture [Jiang et al., 2007] and for heterogeneous catalysis in confined microporous systems [Lu et al., 2015]. Shorter chain length monodisperse oligomers have been studied both as model systems to elucidate the properties of polymers [Martin & Diederich, 1999] and as single molecular wires in molecular electronics and nanotechnological devices. In particular,

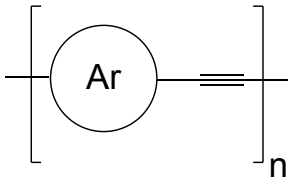

Scheme 1

OAEs as prototypes of rigid-rod π-conjugated systems have been extensively explored in single molecular junctions [Gantenbein et al., 2017], and it has been shown that the optical and conductance properties of both OAEs and PAEs strongly dependent on the dihedral angle between successive arylene units, with coplanar configurations leading to maximized conjugation [Montali et al., 1998] (similarly to what is observed for oligo-paraphenylene units [Venkataraman et al., 2006]) and hence to red shift in absorption and emission and to intra-chain ambipolar charge transport of the order of 10^{-3} $cm^2 \times V^{-1} \times s^{-1}$ [Montali et al., 1998].

The synthesis of PAEs mainly relies either on Sonogashira-type [Sonogashira, 2002] cross coupling of terminal alkynes and aryl halide monomers or on alkyne metathesis [Martin & Diederich, 1999; Bunz, 2000; Bunz, 2005; Advances in Polymer Science, 2005; Ortiz et al., 2017; Montali et al., 1998], with the latter providing more control on the linearity and of the defectiveness of the resulting polymers (side reactions leading to branching are common in cross coupling), but somewhat hindered by the relatively scarce development of new alkyne metathesis catalysts [Montali et al. 1998]. More complex strategies are required to prepare and purify monodisperse OAEs, such as the iterative divergent/convergent binomial synthesis originally reported by Tour et al. [Schumm et al., 1994, Jones II et al., 1997]. All these approaches share a multi-step nature requiring separation and purification, with the additional problems of the generally low solubility of OAEs and PAEs, which makes the functionalization of aryl units with side chains mandatory. Moreover, it is well known that in solution only lower molecular weight PAEs exhibit rigid rod-like structures, while at chain lengths exceeding approximately 15 nm (about 20 repeating units) the linear conformation breaks down leading to worm-like random coil structures [Cotts et al., 1996]. For all these reasons, a new and simpler one-pot synthetic approach producing defect-free, unsubstituted chains maintaining length-independent chain linearity and possibly a high degree of spatial orientation and periodicity is highly desirable in the field of advanced applications in molecular (opto)electronics.

One such approach is provided by OSS, which in recent years has shown an enormous potential in providing efficient synthetic routes – often catalyzed by the substrate – alternative to solution chemistry, and has led to a wealth of surface-supported covalently linked carbon nanostructures [Gourdon, 2008; On-Surface

Synthesis, 2016; On-Surface Synthesis, 2018]. In this field, the research on the on-surface formation of acetylenic scaffolds is comparatively recent and has been prompted by the interest for 1D carbine [Casari et al., 2016] and 2D graphyne and graphdiyne structures [Li et al., 2014], whose common structural motif is the triple bond between two sp-hybridized carbon atoms. The reaction most often employed to link monomers containing the ethynyl functional group is the dehydrogenative homocoupling of terminal alkynes reminiscent of the Glaser-Hay reaction [Zhang et al., 2012; Gao et al., 2013], with the resulting formation of a butadiyne bridge. This strategy has, however, several drawbacks stemming from the high reactivity of terminal alkynes, which leads to poor chemo- and regioselectivity due to several side reactions (cis/trans hydrogenation, insertion, cyclotrimerization, etc.) and ultimately results in the formation of a mixture of short-chain, branched and irregular oligomers [Zhang et al., 2012; Gao et al., 2013; Eichhorn et al., 2013; Cirera et al., 2013]. A certain degree of control on the selectivity can be exerted by carefully choosing the crystallographic orientation of the substrate [Liu et al., 2015], but the best results to date in the growth of a linear PAE by on-surface synthesis have been obtained through the aid of vicinal surface templating, with measured linear chain maximum lengths of 27 nm and 40 nm for graphdiyne wires on Ag(887) [Cirera et al., 2014] and Ag(455) [Klappenberger et al., 2018], respectively. A very recent alternative approach consisting in direct in situ formation of triple C-C bonds through on-surface dehalogenative homocouplings of tribromometyl-substituted arenes [Sun et al., 2018] seems to bear promising potential in the production of extended linear PAEs.

In this former case of study, we report the experimental and theoretical results pertaining to the alternative attempt of growing ordered arrays of long chain linear PAEs based on the well-established Ullmann-like aryl halide homocoupling reaction, which has been extensively used in on-surface synthesis in the last decade [Goudon, 2008; Lipton-Duffin et al., 2009; Eichhorn et al., 2014]. Instead of using highly reactive terminal alkynes as in Glaser-type couplings, we resort to 1,2-bis(4-bromophenyl) ethyne (DBPE, **1**) molecules (see Fig. 3.1.1) as molecular precursor, wherein the acetylenic functional group is internal rather than terminal, being linked to two phenyl groups, each bearing a Br atom in para position.

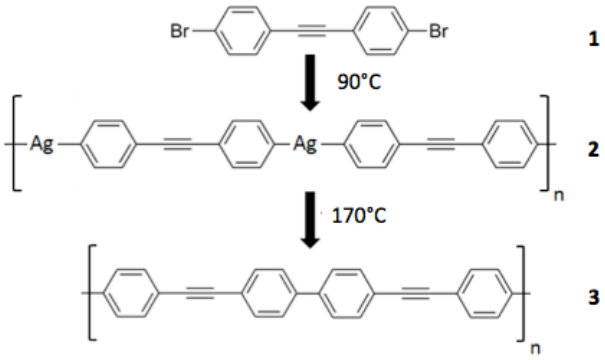

Figure 3.1.1 Schematic representation of longitudinal polymerization of DBPE (**1**) molecules via organosilver intermediate **2** into PAE wires **3**.

The latter are easily detachable by the catalytic role exerted by a metallic substrate [Fan et al., 2015]. We show that **1** deposited and carefully annealed on Ag (110) leads to the production of linear and long range-ordered poly(para-biphenyleneethynylene) (**3**) polymeric wires more than 100 nm long through a two-step synthesis involving the organosilver nanowire (**2**) as an intermediate. We also show that a key role in the successful outcome of the synthetic strategy is played by Br atoms detached from **1** in the first step of the Ullman-like synthesis: by residing on the substrate they keep apart the growing nanowires with a twofold effect: they both direct the linear growth of the polymeric chains and limit the access to (i.e. protect) the C≡C triple bonds within the chain, thereby substantially enhancing the reaction's chemo/regioselectivity by preserving its essentially topotactic nature [Lotgering, 1959, Günther & Oswald, 1975]. In fact, Br desorption at higher temperatures unfetters the reactivity of alkynyl functional groups, leading to a highly branched, amorphous structure.

Methodology: Periodic DFT calculations have been performed by exploiting the QE suite of codes [Giannozzi et al., 2009] and by adopting the Perdew-Burke-Ernzerhof (PBE) exchange–correlation (XC) functional [Perdew et al., 1996]. Valence orbitals were expanded in a plane-wave basis set with a kinetic energy cut-off of 30 Ry, while the interaction between ion cores and valence electrons has been modelled by means of ultrasoft pseudopotentials [Vanderbilt, 1990]. The cut-off on the charge density was 240 Ry. Brillouin-zone (BZ) [Brillouin, 1930] integrations were limited to the Γ-point and a smearing parameter of 0.02 Ry for the electron population function was considered [Marzari et al., 1999]. Numerical experiments have been carried out with and without the inclusion of the dispersion corrections (by taking advantage of the

semi-empirical dispersion-correction scheme developed by Grimme [Grimme, 2006b] and implemented in QE by Baroni and Giannozzi [Baroni & GIannozzi, 2009]). Scanning tunneling microscopy (STM) images have been modelled by using the TH approximation [Tersoff & Hamann, 1985]. Finally, molecular graphics were generated by using the XCRYSDEN graphical package [Kokalj, 1999; Kokalj & Causà, 2000]. Two different sets of numerical experiments have been performed to reproduce the low temperature (LT; organosilver polymer **2** in Figure 3.1.1) and the high temperature (HT; polymer **3** in Figure 3.1.1) phases. In both cases, the Ag(110) surface were modelled by a cell containing five layers, where the top three have been allowed to relax, while the others were kept fixed at their bulk positions. The vacuum region between repeated image along the z direction was large enough to prevent interactions (ca. 16 Å). A bulk optimized lattice parameter of 4.16 Å has been used, which slightly overestimated (1.7%) the experimental value of 4.09 Å [Lide, 2009], but in perfect agreement with other generalized gradient approach calculations [Kokalj et al., 2002; Wang et al., 2001]. Indeed, the dimensions of the two units cells are sensitively different: a unit cell $9.75 \times 13.79 \times 21.84$ Å^3 including 80 atoms has been employed for the low temperature (LT) system (see Figure 3.1.2a), while the dimensions of the latter unit cell are $16.63 \times 45.83 \times 21.84$ Å^3, which includes 277 atoms (see Figure 3.1.2b, where each unit cell contains four debrominated monomers).

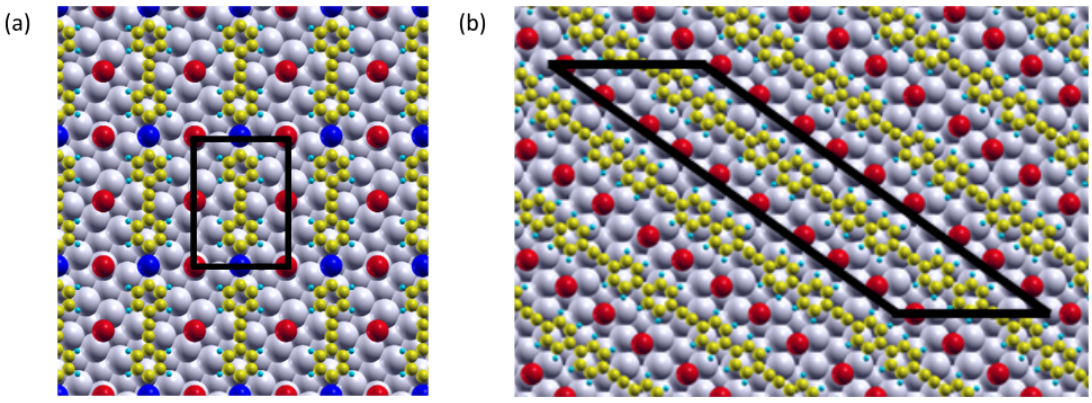

Figure 3.1.2 Ball models for supported (a) LT phase (organosilver polymer **2**) and (b) HT phase (PAE **3** nanowires). Unit cells are outlined by black lines. Color code in models: Br red, C yellow, H light blue, Ag adatoms dark blue, Ag substrate grey.

LT-phase numerical experiments: In the LT phase, major structural variations associated to the presence/absence of dispersion corrections are observed for carbon and hydrogen atoms, while structural parameters of Br atoms are negligibly perturbed.

Indeed, as clearly reported in Figures 3.1.3a and 3.1.3b, the ligand is strongly curved when dispersion corrections are neglected.

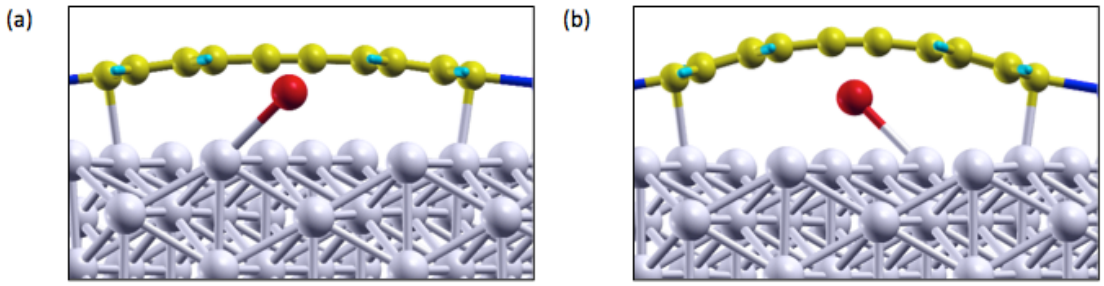

Figure 3.1.3 Side view of the LT phase ball and stick models (a) with and (b) without dispersion corrections.

The distance of C≡C bonds from the surface is 2.76 Å (3.34 Å) when dispersions are (are not) considered. Incidentally, the reduction of the adsorbate/substrate average distances with the inclusion of the dispersion corrections is often reported in the literature for the PBE XC [Ruiz et al., 2016; Toyoda et al., 2010], also for the Ag (110) surface [Ruiz et al., 2016].

Experimental (Figure 3.1.4a) and simulated (Figures 3.1.4b and 3.1.4c) STM images of the LT phase on Ag(110) are displayed in Figure 3.1.4. The agreement between theory and experiment is satisfactory in both cases: i) the Br atoms are brighter than carbon atoms, ii) there is an evident brightness variation for on-top Br atoms when compared to those occupying long-bridge positions (see the white and grey dots in Figures 3.1.4b and 3.1.4c, which are the Br atoms in on-top and long-bridge sites, respectively), and iii) the Ag adatoms are generally brighter than the carbon atoms and their brightness is comparable with that of the on-top Br atoms.

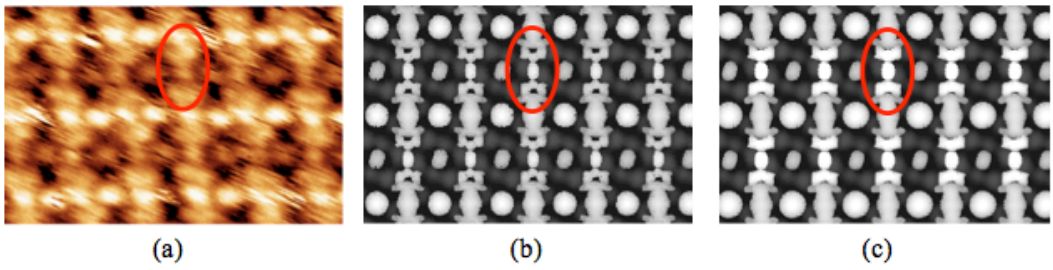

Figure 3.1.4 (a) Experimental and simulated STM images (b) with and (c) without the inclusion of dispersion corrections for the LT phase at a bias voltage of V = -0.6 V.

Nevertheless, a careful comparison of experimental and simulated STM images with and without dispersion corrections (see Figures 3.1.4b and 3.1.4c) demonstrates that the image without corrections overestimates the adsorbate-substrate distance (see the red oval in Figure 3.1.4c, which highlights that the brightness of the ethynyl carbon atoms is comparable to that of the Br atoms). This in not observed in the experimental image (see red oval in Figure 3.1.4a). In agreement with the experimental evidence, carbon atoms in the red oval of Figure 3.1.4b are less bright than the Br atoms.

HT-phase numerical experiments: Optimized structures obtained with and without dispersion corrections are displayed in Figure 3.1.5. The inspection of Figures 3.1.5a and 3.1.5b, reveals that, differently from the LT phase, the inclusion of dispersion corrections has minor effects: the polymer remains in its flat conformation in both cases. The most evident variation is the average distance of the polymer from the surface, which is smaller (~ 0.5 Å) when adopting the dispersion corrections approach.

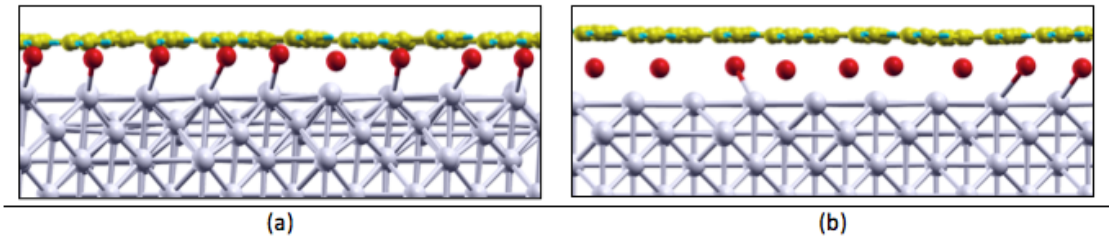

Figure 3.1.5 HT phase ball and stick models (a) with and (b) without dispersion corrections.

Also the STM images of the HT phase are simulated with and without dispersion corrections. Figure 3.1.6 includes the experimental image (Figure 3.1.6a), recorded at a bias voltage of -1.0 V, as well as the simulated ones (Figures 3.1.6b and 3.1.6c). The agreement between experiment and theory is satisfactory in both cases. In particular, simulated images correctly reproduce the following evidences: i) polymer chains are brighter than Br atoms, and ii) despite all Br atoms are in hollow positions, their brightness is different. The only relevant difference between the two calculations is the overestimated brightness of polymer chains when the dispersion corrections are neglected. The simulation with dispersion corrections included is more similar to the experimental image. Hence, similarly to the LT phase, the simulated STM image with dispersions included better fits the experimental ones, even though differences between the two approaches are less evident for the HT phase.

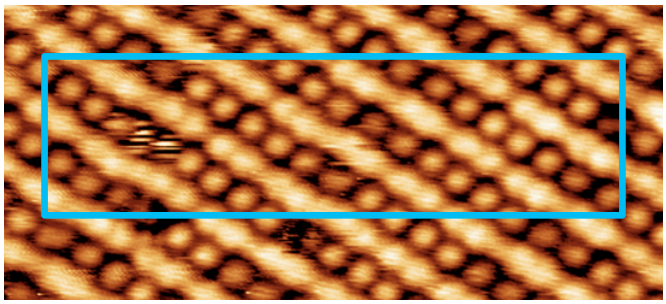

(a)

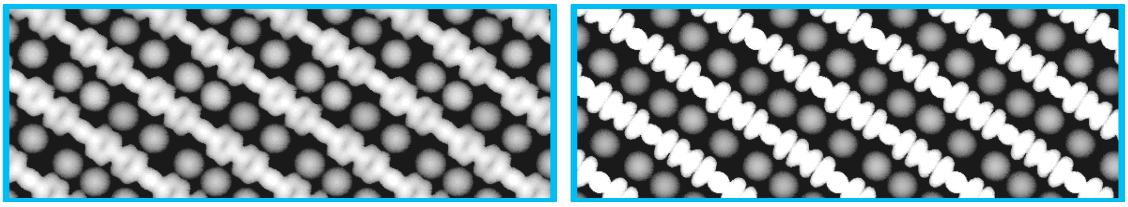

(b) (c)

Figure 3.1.6 (a) Experimental and simulated STM images (b) with and (c) without the inclusion of dispersion corrections for the HT phase at a bias voltage of V = -1.0 V.

Löwdin analysis for LT/HT optimized geometries with dispersion corrections: Further information about the nature of the adsorbate-substrate interactions and the role of the Br atoms can be obtained by exploiting the Löwdin charge analysis [Löwdin, 1950; Szabo & Ostlund, 1996], which has been limited to the results obtained with the inclusion of dispersion corrections. This analysis was used to determine the charges on different carbon atoms in different systems (see Table 3.1.1): i) isolated molecule (ISO), ii) LT phase, iii) LT phase without Br atoms (LT*), iv) HT phase and v) HT phase without Br atoms (HT*). The inspection of data collected in Table 3.1.1 for the LT phase reveals that carbon atoms are usually negatively charged with respect to the isolated molecule (ISO); moreover, C_5 are the most negatively charged carbon atoms. C_5 of the LT* system have the same charge values, thus stressing the negligible effect of the Br atoms on the ligand. The carbon atoms (C_1 and C'_1) involved in the triple bond do not undergo significant charge variations and this is supported by the negligible variation of the triple bond length (1.2196 Å *vs* 1.2208 Å, for the isolated and LT supported system, respectively). The charge analysis for the HT and HT* systems reveals i) the same negligible effects of Br atoms on the charge of carbon atoms and ii) a not significant charge variation for carbon atoms (C_1 and C'_1) involved in the triple bond with respect to the isolated molecule (bond lengths 1.2196 Å *vs* 1.2348 Å, for the isolated and HT supported system, respectively).

Table 3.1.1 Average total Löwdin charge analysis (in units of *e*) for the C atoms of isolated molecule and average triple bond lengths (in Å) for low and high temperatures 2D patterns. Systems with (*) contain only the molecular systems without Br atoms in their optimized geometries. All the charges are reported for the calculations with the inclusion of the dispersion correction.

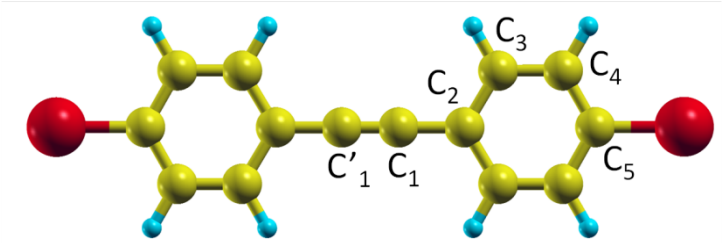

	C_1	C_2	C_3	C_4	C_5	C'_1-C_1
ISO	3.983	3.958	4.085	4.104	4.004	1.220
LT	4.004	3.970	4.113	4.131	4.396	1.221
LT*	4.004	3.968	4.112	4.115	4.393	1.220
HT	4.000	4.004	4.109	4.122	3.961	1.235
HT*	4.002	3.973	4.106	4.118	3.965	1.236

The more relevant variations with respected to the isolated molecule are observed for C_5 atoms, which were negatively charged in LT (+0.39*e*) and slightly positively charged in HT (-0.04*e*). This difference is due to the different atom involved in the bond with C_5: an Ag adatom in the former and a phenyl ring in the latter case.

Results and Discussion: STM-images reported in Figure 3.1.7 show the as-deposited structure of **1** on the Ag (110) surface. The large-scale image (Figure 3.1.7a) reveals that the surface is almost fully covered by the molecules. The deposition is self-limiting at LT: by increasing the deposition time the on-surface amount of the precursor, estimated by the X-ray Photoelectron Spectroscopy (XPS) C 1s peak area, does not increase after the completion of the first monolayer (ML). A closer inspection of Figure 3.1.7a reveals that the molecules are organized in two separate domains aligned along the $[1\bar{1}3]$ and $[\bar{1}13]$ directions (highlighted by blue arrows), which are symmetrically equivalent with respect to the substrate [001] main direction (denoted by the vertical black arrow). Already at LT, molecules react to form organosilver nanowires **2**. As well known for the surface synthesis starting from brominated organic molecules deposited on silver substrates [Chung et al., 2012; Fan et al., 2018], Br atoms detach from the precursor due to the substrate-catalyzed homolytic C-Br bond cleavage and silver adatoms replace them, forming C-Ag-C bonds. At LT, however, ordered domains are formed by organosilver wires composed

by only few monomers, and often quite disordered areas are found. Annealing for 1 hour at 90 °C, as reported in Figure 3.1.7b, increases the order of the organometallic phase, but at the same time decreases the surface coverage due to molecular desorption. To increase the dimensions and the regularity of the domains, we therefore performed the annealing at 90 °C under the deposition flux of **1**. The equilibrium between desorbed and adsorbed molecules allowed us to obtain a well-covered surface with large domains, as reported in Figure 3.1.7c.

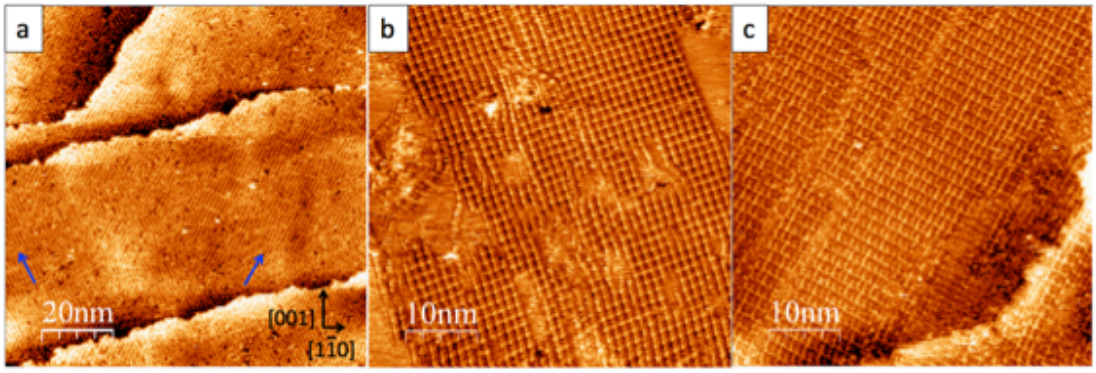

Figure 3.1.7 (a) (100 × 100 nm^2, V = -0.6 V, I = 1.5 nA) Self-assembly of the as-deposited DBPE molecules; blue arrows indicate the directions of the two symmetrically equivalent domains; (b) (50 × 50 nm^2, V = -0.2 V, I = 0.5 nA) after annealing at 90°C in UHV; (c) (50 × 50 nm^2, V = -0.5V I = 5 nA) after annealing at 90°C in atmosphere of **1**.

Figure 3.1.8 shows the STM images of the organosilver phase (hereafter: low temperature, LT phase) obtained upon deposition of **1** on Ag (110) in the described conditions, as well as the proposed model and the DFT simulation of the STM image. On the basis of the Low Energy Electron Diffraction (LEED) pattern (not herein reported), the unit cell orientation and dimensions of the model (see also Figure 3.1.2) correspond to a commensurate superlattice expressed by the $[3 \pm 1, 2 \mp 3]$ matrix notation. As shown in the model reported in Figure 3.1.8, the Br atoms (red spots) detach from opposite ends of **1** and silver adatoms (blue spots) replace them, thereby creating the organosilver wires **2**. The dissociated Br atoms remain adsorbed on the Ag substrate and diffuse to two precisely identifiable positions: (a) between two Ag adatoms belonging to adjacent organosilver wires and (b) in the free space between two nearby C≡C triple bonds. The image reveals that the former appear brighter than the latter. To understand the nature and the role of the different atoms involved in the supported system and to rationalize the different Br contrast in the STM image,

supercell DFT numerical experiments by using the Quantum-ESPRESSO package have been carried out [Giannozzi et al., 2009].

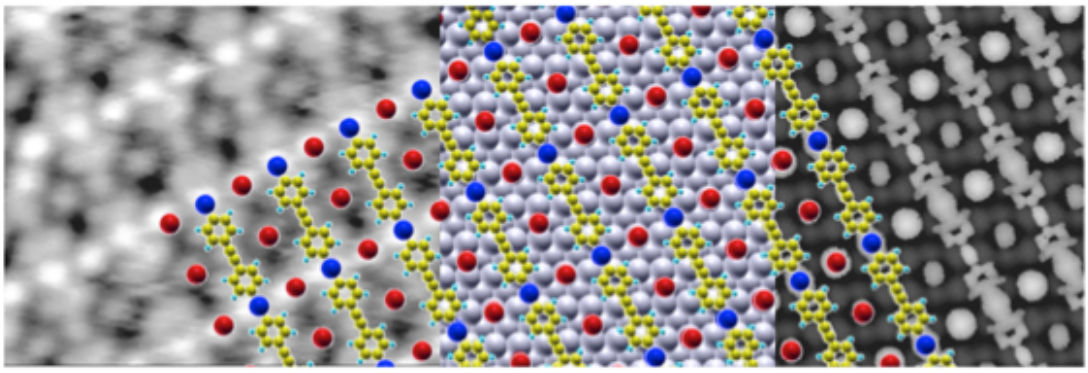

Figure 3.1.8 Experimental STM (6×5 nm^2, V = -0.7 V, I = 12 nA) of the LT phase, consisting of organosilver polymer **2** obtained by deposition of **1** on Ag (110) at 90°C (left); ball-and-stick model: Br red, C yellow, H light blue, Ag adatoms dark blue, Ag substrate grey (center); DFT simulation of the experimental image (right, see text for details).

DFT simulations correctly reproduce the STM image and important information on the geometry of the system can be inferred: i) there is an evident brightness variation for Br atoms, which is correlated with the different absorption site they occupy on the Ag substrate, with darker Br atoms on long-bridge positions (halfway the long side of the rectangular Ag(110) surface unit cell), and with the brighter ones on-top of Ag substrate atoms; ii) on-top Br atoms are brighter than carbon atoms, and iii) Ag adatoms are generally brighter than carbon atoms and their brightness is comparable with that on the on-top Br atoms. Further information about the nature of the adsorbate-substrate interactions can be obtained by exploiting the Löwdin charge analysis (see Table 3.1.1). With respect to the isolated molecule, the supported C atoms are negatively charged, with a strong prevalence of the charge on the carbon atoms involved in the bond with Ag adatoms (C_5 in Table 3.1.1). It is noteworthy that the Br atoms negligibly affect the charge distribution on the carbon atoms of monomers.

The second step of the synthesis consists in annealing the LT phase at 170 °C (HT phase) for 45 minutes under deposition flux of **1** (Figure 3.1.9). Large scale and high resolution STM images (Figures 3.1.9a and 3.1.9b, respectively) reveal that this causes the release of the Ag adatoms, with the production of an ordered array of poly(para-biphenyleneethynylene) polymeric wires **3** more than 100 nm long that covers the whole surface (The DFT optimized model is reported in Figure 3.1.9c).

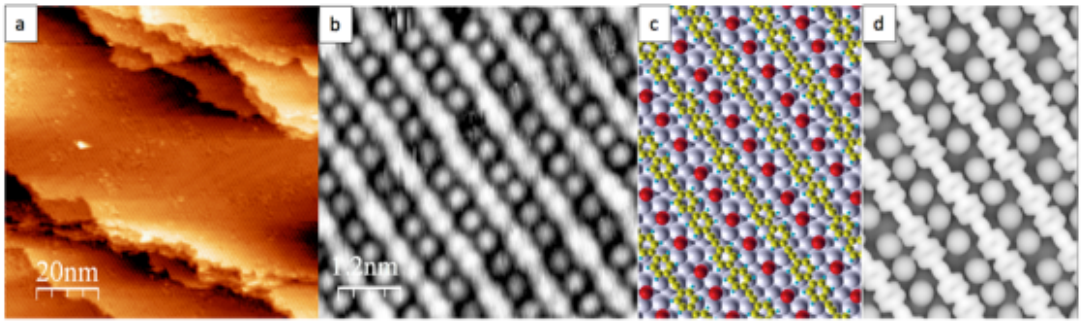

Figure 3.1.9 Experimental STM of organic nanowires **3** obtained after annealing at 170 °C (a) large scale (100 × 100 nm^2, V = 0.23 V, I = 4.3 nA) , (b) small scale (6 × 6 nm^2, V = -1.1 V, I = 12 nA); (c) ball-and-stick model: Br red, C yellow, H light blue, Ag substrate grey; (d) DFT simulation of the experimental image (right, see text for details).

The length of each building block of **3** is about 1.1 nm, which is consistent with a repeat unit formed by a triple C≡C bond sided by two phenyl rings. The STM contrast of the organic part is well reproduced by the DFT simulation reported in Figure 3.1.9d. The Br atoms are still in-between the nanowires and give rise to a fairly regular alternation of brighter and dimmer spots, a feature that is also well reproduced by DFT simulations. Polymeric wires do not show any clear sign of commensuration with the substrate. For this reason, the long unit cell 16.63 × 45.83 × 21.84 $Å^3$ including 277 atoms has been considered to simulate the surface structure (see Figure 3.1.2b). It has been already mentioned that, differently from the LT system, the inclusion of the dispersion corrections has only minor effects: in both cases the polymer retains the flat conformation (see Figure 3.1.5). Moreover, similarly to LT theoretical outcomes, the most evident variation is the polymer/surface average distance, which is smaller (~ 0.5 Å) when dispersion corrections are included, resulting in a better reproduction of the STM contrast. Despite the larger dimensions of the unit cell, the interpretation of DFT calculations for the HT phase is definitely more straightforward: long polymeric wires are separated by Br atoms, all residing in hollow surface sites (see Figure 3.1.9c). It should be noted that these Br atoms are not equally distributed along the wires: their positions are not equivalent both with respect to the surface (from a minimum vertical distance of 1.54 Å to a maximum of 1.95 Å, the average value within the unit cell being 1.77 Å) and to the polymer. This is evident in the STM experimental image (Figure 3.1.9b) and it is correctly reproduced by the DFT model (Figure 3.1.9d), which confirms that the different

heights of the Br atoms are responsible for their different brightness. Similarly to the LT system, the Löwdin charge analysis reveals the negligible effects of Br on the charge distribution on the polymer carbon atoms. More specifically, when moving from the LT to the HT phase all but one carbon atoms are characterized by substantially the same charge density. The exception corresponds to the C_5 atom (see Table 3.1.1), which in **3** is bonded to a phenyl ring, while in **2** was bonded to an Ag adatom.

Interestingly, the DFT-optimized polymeric chain structure shows that biphenylene units within the chain lie flat on the Ag (110) surface, i.e. the dihedral angle both between nearest neighbor phenyl rings within a biphenyl unit and between successive biphenyl units is zero within ±2° (see the side views in Figure 3.1.5). This is different from what is found for polyparaphenylene (PPP) wires supported on weakly interacting Au (887) [Basagni et al., 2016], where the dihedral angle between successive phenyl rings was measured to be 40° ± 10°, and similar to PPP on the much more strongly interacting Cu(110) [Di Giovannantonio, 2013]. The twisted conformation of the para-linked phenylene units is due to the steric hindrance between the orto hydrogen atoms of neighboring phenyl rings [Ambrosch-Draxl et al., 1995; Sasaki et al., 1992], which is counteracted by the vertical polymer-substrate interaction. In wire **3** such steric hindrance is halved with respect to PPP due to the insertion of ethynyl units among biphenylene units. The resulting flat conformation maximizes the 1D polymer conjugation and should therefore reduce the optical band gap with respect to twisted conformations. The DFT Highest Occupied Molecular Orbital (HOMO) – Lowest Unoccupied Molecular Orbital (LUMO) ΔE of unsupported **3**, calculated for a molecule with 16 phenyl rings to prevent the dependence of the electronic structure from the length of the oligomer, amounts to 1.79 eV at the Γ point of the first BZ, which is reduced to 1.49 eV for the surface-supported polymeric wire. The value for unsupported PPE is 1.63 eV.

Further information on the reaction sequence as a function of temperature is provided by XPS measurements: results for C 1s and Br 3d peaks from LT and HT phases are compared in Fig. 3.1.10.

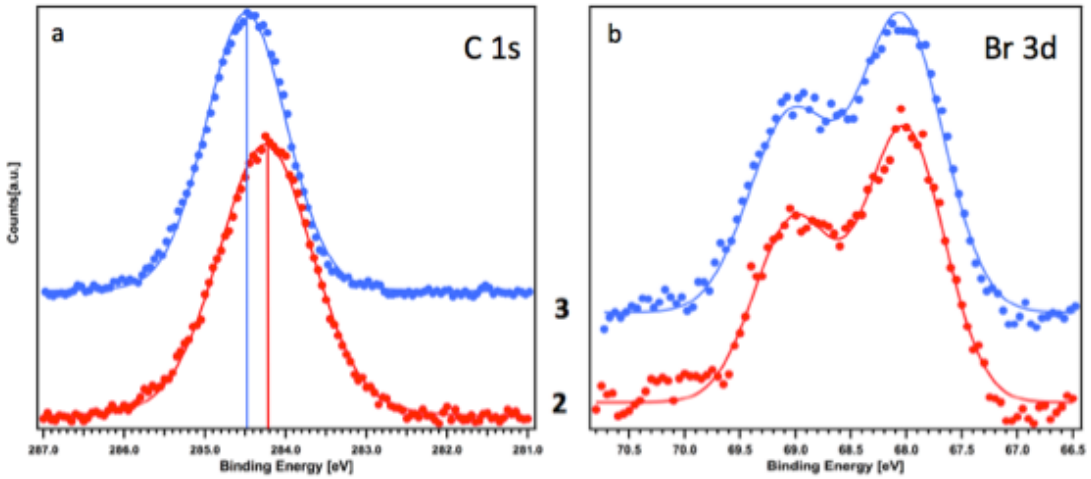

Figure 3.1.10 Experimental and fitting of (a) C 1s and (b) Br 3d XPS peaks of the organosilver wires **2** obtained after annealing at 90 °C (LT phase) and of the PAE wires **3** obtained after annealing at 170 °C (HT phase).

Both the Br 3d peaks have the 5/2 component centered at 68.0 eV (Fig. 3.1.10b), confirming that all Br atoms are adsorbed at the surface, whereas the C 1s peak shifts from a BE of 284.2 eV (Fig. 3.1.10a) for the organosilver wires, characterized by the C-Ag bonds, to 284.5 eV after the annealing, due to the release of the Ag atoms and the formation of direct C-C bonds between the molecular building blocks [Píš et al., 2016]. The spectra obtained from molecules deposited at LT (not shown) are identical to those reported after the annealing at 90 °C, confirming that the organosilver wires **2** are already formed at LT and that the annealing at 90 °C only increases the surface order.

The combined use of the experimental and computational results suggests that Br atoms detached from the molecular precursor act as spacers between the organometallic wires, thus preventing the interaction between nearest neighbor triple bonds and collectively playing the role of a "rail" for the longitudinal self-assembly of the wires. Comparative experiments performed on Au(111) (see Figure 3.1.11) have evidenced how – due to the lower absorption energy of Br atoms on gold – on that surface only a mesh of interconnected nanowires can be obtained. Indeed, already at 170 °C the C≡C triple bonds start to react, forming an interlinked network of nanowires aligned along different directions. From a computational point of view, the role of Br atoms as spacers between wires is supported by the Löwdin charge analysis for the LT and HT phases, with and without the presence of the Br atoms. In both cases, the partial charges residing on C atoms are negligibly affected by the presence

of Br. This finding supports the hypothesis that Br atoms play a "physical" (spacer) rather than a "chemical" (electronic interaction) role.

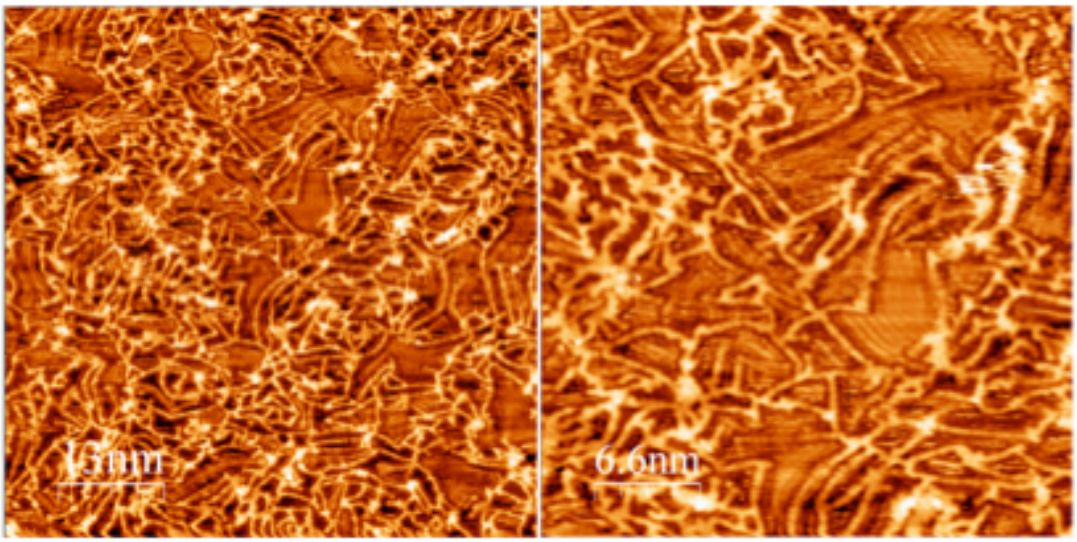

Figure 3.1.11 STM images. (left) (65 × 65 nm^2) and (right) (33 × 33 nm^2), V = 1.1 V, I = 0.8 nA. 2D DBPE-based amorphous polymers obtained on Au(111) at T = 170 °C.

At temperature higher than 320 °C Br atoms start to desorb, as revealed by the decrease of the area of the Br $3d_{5/2}$ peak in XPS. The effects of Br desorption from the surface are shown in Figure 3.1.12. In Figure 3.1.12a the PAE wires maintain the uniaxial order as long as Br atoms stay in place (blue arrow), but – given their high flexibility [Ortiz et al., 2017], even on-surface [Cirera et al., 2014] – they start to link to each other as soon as Br leaves the surface. Yellow circles evidence x-shaped links that seem to point to a [2 + 2] cycloaddition of two alkynyl groups belonging to adjacent wires (a reaction that has been recently claimed for the on-surface coupling of pyrene moieties [Tran et al., 2017] and that is known to be catalyzed (and the resulting cyclobutadiene unit stabilized) by transition metals [Schore, 1988]. However, given the complex chemistry of alkynes, which can undergo metathesis, insertion, cyclization, hydrogenation reactions to name but a few, most often the onset of Br desorption is accompanied by a degradation of the starting order, leading to the formation of small oligomers linked in many different geometries. In addition, Figures 3.1.12b and 3.1.12c show how, by increasing the temperature to 350 °C, Br atoms completely desorb, thereby allowing lateral reactions between the nanowires to occur on the whole surface. The final result is an amorphous bi-dimensional short-branched mesh with no preferential growth direction compared to the starting ordered

1D PAE wires array. It is instructing to compare this finding with what has been observed starting from 4,4″-dibromo-p-terphenyl molecules, where no triple bonds are present: the graphene nanoribbons developing by lateral fusion of PPP polymers, initially produced by the 1D Ullmann-like polymerization of the precursors, display a clear azimuthal orientation reminiscent of the order of starting PPP nanowires [Basagni et al., 2015].

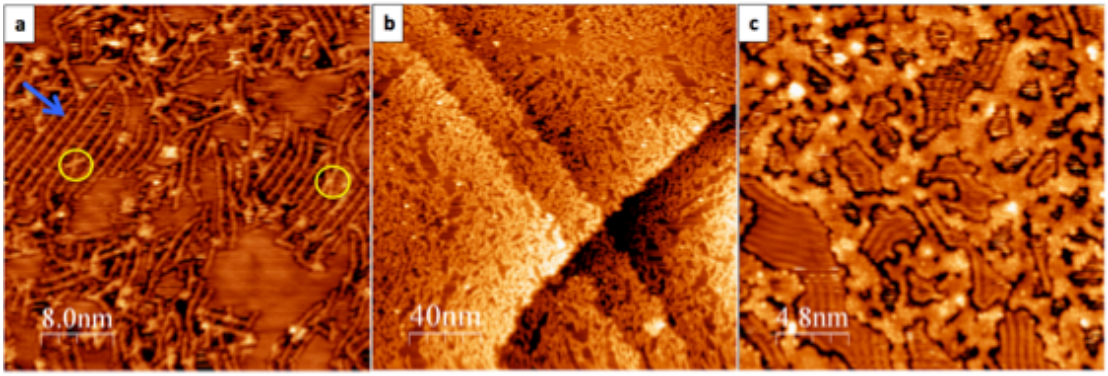

Figure 3.1.12 STM images. (a) (40 × 40 nm^2, V = 1.5 V, I = 0.2 nA) onset of the 2D linking of PAE nanowires (T = 320 °C): the blue arrow shows ordered nanowires, yellow circles indicate x-shaped links between adjacent nanowires; (b) (200 × 200 nm^2, V = -0.7 V, I = 0.3 nA) and (c) (24 × 24 nm^2, V = 0.8 V, I = 8 nA) 2D DBPE-based amorphous polymers (T = 350 °C).

As already remarked, up to now the bottom-up synthesis of PAE wires by means of on-surface synthesis has mostly relied on Glaser-like homocoupling of terminal alkynes [Zhang et al., 2012; Gao et al., 2013; Eichhorn et al., 2013; Cirera et al., 2013], although dehalogenative homocoupling of tribromomethyl-substituted arenes has recently emerged as a possible alternative [Sun et al., 2018]. The high reactivity of terminal alkynes requires a strict control of the chemo- and regioselectivity of the coupling reaction, which can be achieved by exploiting the templating effect of vicinal surfaces [Cirera et al., 2014], possibly further enforced by the smart functionalization of molecular precursors, affording specific directional intermolecular interactions capable of properly orienting the monomers [Klappenberger et al., 2018]. Surface templating by regular monoatomic step arrays poses, however, limits the achievable polymeric surface density (in principle one polymeric wire or double strand per step) and affords only approximate linearity due to the irregularities in the step edge profiles.

Conclusions: In this former case of study it has been shown that a long-range ordered, dense arrays of highly linear and extremely long PAE wires can be grown without relying on substrate templating if Ullmann-like homocoupling of alkynyl-containing bromo-arenes such as DBPE (**1**) is carried out on Ag (110). In the past, the permanence of Br detached from molecular precursors in on-surface Ullmann-like homocoupling reactions has been often identified as a limiting factor in the growth of ordered polymeric nanostructures produced by Ullmann coupling, since it usually influences the diffusion of reacting monomers and hampers the formation of regular covalent bonds [Tran et al., 2017; Pham et al., 2016]. For this reason Br removal by hydrogen dosing during the activation of the on-surface reaction has been recently proposed [Bronner et al., 2015] and successfully employed [Tran et al., 2017].

Surprisingly, in the present case Br adatoms detached from the molecular precursor, far from degrading the quality of the on-surface grown polymeric wires, play an active role in the successful outcome of the synthesis. In fact, in the initial stages of the reaction Br adatoms act as spacers between adjacent organosilver nanowires with a twofold effect: they both increase the reaction's chemo/regioselectivity by avoiding the interaction between adjacent C≡C triple bonds (i.e. they have the role of protecting groups) and also provide a directing effect for their 1D growth. The organosilver nanowires are then topotactically transformed into ordered and oriented all-organic 1D linear polymers by annealing at 170 °C. This occurs by elimination of the Ag adatoms from the initial organosilver nanowires, with contextual formation of direct C-C links between successive monomeric precursors, with Br atoms still retaining their role in controlling the selectivity and directing the growth. Only at much higher temperature (320 °C) enough thermal energy is provided to initiate Br desorption. This in turn allows C≡C triple bonds on adjacent polymeric wires to approach each other, react and form an amorphous surface-supported 2D oligomeric mesh. DFT calculations provide an excellent fit to the STM images of the polymeric strands, and in particular show that the byphenylene units within the polymeric scaffold lie flat on the surface, which maximizes the electron conjugation along the PAE wires.

Case Study n° 2

3.2 An experimental and theoretical study of a metallorganic coordination networks of tetrahydroxyquinone on Cu(111).

Introduction: The adsorption of single molecular units on clean surfaces, the earliest step to fabricate surface-supported supramolecular structures, is one of the most promising ways for obtaining novel, two-dimensional (2D) ordered metal-organic architectures [Dong et al., 2016] with unique and peculiar structural features, functionalities, and catalytic properties [Ecija et al., 2012; Stepanow et al., 2004; Kudernac et al., 2009; Grumelli et al., 2013; Dmitriev et al., 2003; Rosseinsky, 2004; Perepichka & Rosei, 2007]. In this way, single metal atoms embedded into an organic cage [Betti et al., 2012; Fortuna et al., 2012] or small metal clusters [Bebensee et al., 2013; Bebensee et al., 2014] can be obtained in a highly ordered fashion within a quasi-planar 2D molecular lattice. For metals such as gold, clusters made of few atoms often present catalytic properties absent in their bulk counterpart [Hashmi & Hutchings, 2006], and also the chemical reduction efficiency of tetrameric copper clusters has been recently outlined [Liu et al., 2015]. The wide range of applications that need a specific cluster size underlines the importance of developing novel techniques to enable the tuning of material properties. As such, Lo Cicero et al. [Lo Cicero et al., 2017] were able to grow in the near past a highly-ordered array of tetrameric copper clusters coordinated into a metal-organic network by using tetrahydroxyquinone (THQ) (see Figure 3.2.1) as organic SBU. The cluster array was obtained by depositing THQ molecules on the Cu(111) surface held at RT; a thermally activated dehydrogenation with the formation of tetraoxyquinone tetra-

anions (TOQ) having a 4 × 4 periodicity was then produced by exploiting an annealing procedure involving a 20 min heating ramp up to ~ 110 °C followed by 4 min annealing at the same temperature.

In this latter case of study, we have theoretically revisited the results recently published by Lo Cicero et al. [Lo Cicero et al., 2017] to get an even more detailed description of the structural arrangement of the tetrameric copper clusters on Cu(111).

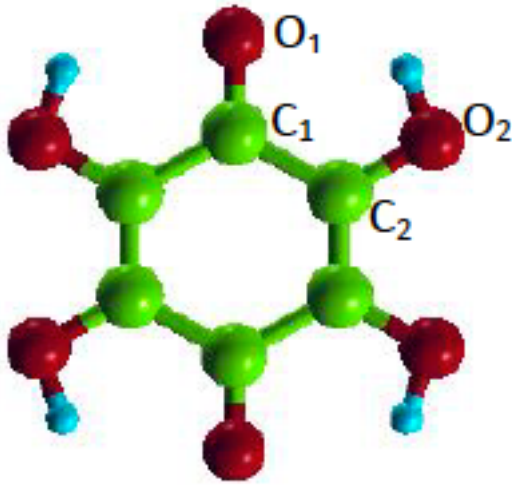

Figure 3.2.1 Ball and stick representation of the tetrahydroxyquinone (THQ) SBU in a planar D_{2h} conformation.

Methodology: Similarly to the modelling of the surface-confined 2D polymerization of the DBPE on Ag(110), the theoretical study of THQ on Cu(111) has been carried out by exploiting the QE suite of codes [Giannozzi et al., 2009] and by adopting the Perdew-Burke-Ernzerhof (PBE) exchange–correlation (XC) functional [Perdew et al., 1996]. Valence orbitals were expanded in a plane-wave basis set with a kinetic energy cut-off of 30 Ry, while the interaction between ion cores and valence electrons has been modelled by means of ultrasoft pseudopotentials [Vanderbilt, 1990]. The cut-off on the charge density was 120 Ry; BZ integrations [Brillouin, 1930] were limited to the 2 × 2 × 1 Monkhorst and Pack mesh [Monkhorst & Pack, 1976]; moreover, a smearing parameter of 0.02 Ry for the electron population function was considered [Methfessel et al., 1989; Marzari et al.1999]. Again, numerical experiments have been carried out either neglecting or including [Grimme, 2006b] dispersion corrections as implemented in QE by Baroni and Giannozzi [Baroni & GIannozzi, 2009]. STM simulations have been modelled by using the usual TH approximation [Tersoff & Hamann, 1985]. In both cases, the Cu(110) surface was modelled by a supercell p(4×

4) containing five layers, where the top three have been allowed to relax, while the others were kept fixed at their bulk positions. The vacuum region between repeated image along the z direction was large enough to prevent interactions (ca. 18 Å). A bulk optimized lattice parameter of 3.66 Å has been used, which slightly overestimated the experimental value of 3.62 Å [Lide, 2009], but in perfect agreement with other generalized gradient approach calculations [Vitos et al., 1998; Kovačević & Kokalj, 2013].

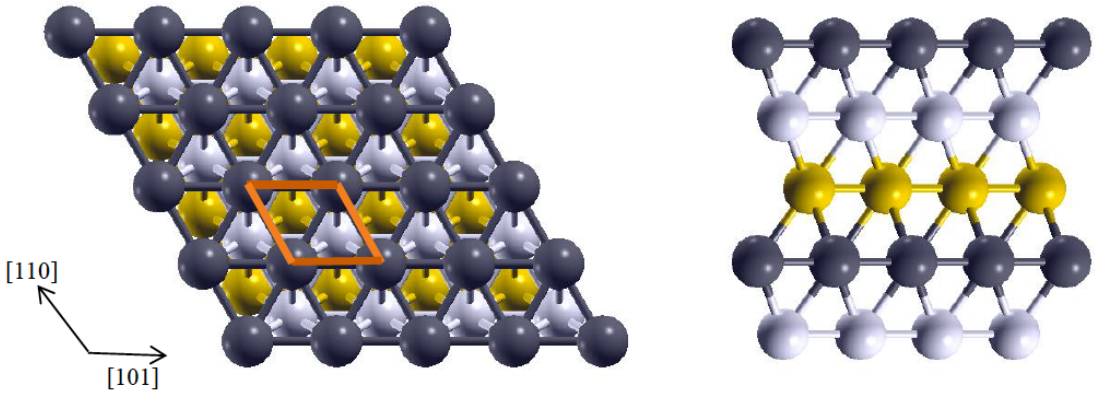

Figure 3.2.2 Top (left) and side (right) view representations of the Cu(111) surface. The surface unit cell is outlined in orange in the left panel. Grey, silver and yellow spheres are representative of the Cu atoms belonging to the first, second and third layers, respectively.

Free THQ optimized structural parameters are compared with corresponding experimental values [Allen et al., 1987] in Table 3.2.1. Numerical experiments have been carried out by adopting a cubic unit cell $20 \times 20 \times 20$ Å^{3,} including (PBE-D2) or neglecting (PBE) dispersive interaction, by using a cutoff of 30 Ry and $2 \times 2 \times 1$ ***k***-point mesh. Results reported in Table 3.2.1 ultimately testify the negligible role played by dispersive interactions when considering the isolate adsorbate.

Table 3.2.1 Optimized geometries (Å) for isolated THQ estimated by adopting either the PBE or the PBE-D2 XC functional. Experimental results have been also included for comparison. Atom labels are those of Figure 3.2.1.

	PBE	**PBE-D2**	**Exp.**[a]
C_1–C_2	1.47	1.47	1.47
C_2–C_2	1.36	1.36	1.34
C_1–O_1	1.24	1.24	1.23
C_2–O_2	1.34	1.34	1.36
O_2–H	0.99	0.99	0.96

[a]Allen, F. H.; Kennard, O.; Watson, D. G.; Brammer, L.; Orpen, A. G.; Taylor, R. *J. Chem. Soc., Perkin Trans. 2*, **1987**, *0*, S1.

THQ adsorption at LT: Diverse possible configurations of THQ@Cu(111) have been considered to determine the relative stability of different adsorption sites (top (T), bridge (B), hollow (H); see Figure 3.2.3). As already mentioned, all the numerical experiments have been carried out by adopting a hexagonal p(4×4) unit cell having dimensions $10.36 \times 10.36 \times 26.46$ Å^3 consisting of 96 atoms on which a single THQ molecule have been initially positioned in a flat geometry at 2.20 Å from the surface [Bebensee et al., 2014; Lo Cicero et al., 2017].

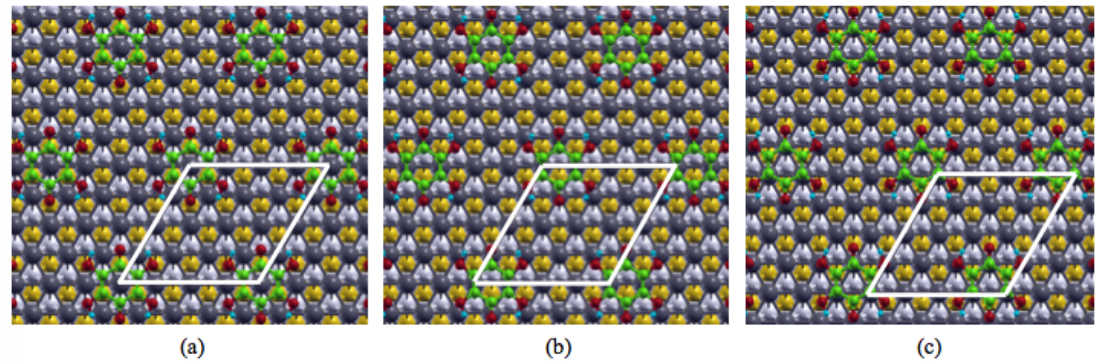

Figure 3.2.3 Schematic representation of THQ@Cu(111): (a) T, (b) B, (c) H. Corresponding unit cells are also displayed. The atom color code is the same of the Figures 3.2.1 and 3.2.2.

Adsorption energy values of THQ@Cu(111) surface are collected in Table 3.2.2.[8]

Table 3.2.2 Adsorption energies (eV) for different THQ chemisorption sites (T, B, H; see text) on Cu(111) (see Figure 3.2.3) including or neglecting dispersive interactions.

Site	PBE	PBE-D2
T	-0.06	-1.42
B	+0.02	-1.73
H	+0.09	-1.69

As expected, and in agreement with data reported by Liu et al. for C_6H_6 on Cu(111) [Liu et al., 2013] and Tonigold & Grob for C_4H_4S on Cu(111) [Tonigold & Grob, 2010], the inclusion of dispersive corrections (PBE-D2) implies adsorption energies significantly larger than those computed by using the PBE XC functional. Moreover, among the diverse chemisorption sites taken into account, the quasi-degenerate B and H ones are the most favoured (see Table 3.2.2).

[8]The adsorption energy has been evaluated as the difference between the total energy of the adsorbate/substrate system and the sum of total energy of the clean slab and the total energy of the isolated adsorbate molecule.

The comparison between free (Table 3.2.1) and chemisorbed (Table 3.2.3) THQ bond lengths ultimately testifies that, independently of the chemisorption site and the inclusion/exclusion of dispersive corrections, the adsorbate structural parameters undergo minor perturbations upon chemisorption.

Table 3.2.3 THQ Bond Lengths (BLs, Å) for T, B and H chemisorption sites. BLs pertaining to the free THQ (THQ^F) have been also included for comparison. Internuclear distances between selected THQ atoms and the Cu(111) surface are also reported. Atom labels are the same of the Figure 3.2.1.

BL	PBE^F	$PBE\text{-}D2^F$	PBE^T	$PBE\text{-}D2^T$	PBE^B	$PBE\text{-}D2^B$	PBE^H	$PBE\text{-}D2^H$
C_1–C_2	1.47	1.47	1.46	1.45	1.43	1.43	1.43	1.43
C_2–C_2	1.36	1.36	1.36	1.37	1.39	1.39	1.40	1.40
C_1–O_1	1.24	1.24	1.25	1.27	1.31	1.31	1.32	1.32
C_2–O_2	1.34	1.34	1.35	1.36	1.36	1.37	1.37	1.37
Cu(111)–C_1			3.37	2.72	2.42	2.34	2.37	2.28
Cu(111)–C_2			3.34	2.75	2.50	2.41	2.45	2.34
Cu(111)–O_1			3.38	2.64	2.39	2.28	2.34	2.26
Cu(111)–O_2			3.31	2.78	2.67	2.58	2.59	2.48

The most relevant structural variation concerns the C_1–O_1 BL, which increases from 1.24 Å (free THQ) to 1.31/1.32 Å (THQ(B)/THQ(H)). In agreement with the PBE-D2 adsorption energies, higher than the PBE ones, the PBE-D2 distances of C and O THQ atoms from the Cu(111) surface are shorter than the PBE ones. It can be of some interest to point out that, even though THQ structural parameters at the T site are substantially unaffected upon chemisorption and, for this reason, they are not herein reported, the opposite is true when the adsorbed-substrate distance is considered (*vide infra*).

Further insights into the THQ–Cu(111) interaction may be gained by taking advantage of the Löwdin charge analysis [Löwdin, 1950; Szabo & Ostlund, 1996] carried out for free and chemisorbed TQH at T, B and H sites (see Table 3.2.4).

Table 3.2.4 Löwdin charges for THQ atoms (free THQ charges in parenthesis). Atomic labels are the same of the Figure 3.2.1.

Atom	PBE^F	$PBE\text{-}D2^F$	PBE^T	$PBE\text{-}2D^T$	PBE^B	$PBE\text{-}D2^B$	PBE^B	$PBE\text{-}D2^B$
C_1	0.30	0.30	0.27	0.18	0.11	0.11	0.11	0.11
C_2	0.19	0.19	0.17	0.13	0.11	0.11	0.11	0.11
O_1	-0.33	-0.33	-0.36	-0.48	-0.54	-0.55	-0.54	-0.55
O_2	-0.33	-0.33	-0.33	-0.35	-0.37	-0.37	-0.37	-0.37
Slab			0.20	0.86	+1.28	+1.30	+1.28	+1.30

The inspection of Tables 3.2.1, 3.2.3 and 3.2.4 clearly indicates that, among THQ heavy atoms, those undergoing the strongest structural and electronic perturbations upon adsorption are C_1 and O_1. This is ultimately due to a substrate → adsorbate charge transfer from Cu d atomic orbitals (AOs) into lowest-lying THQ-based π^*

MOs, antibonding in character with respect to the C_1–O_1 interaction. This charge transfer, more effective for B and H chemisorption sites than for the T one, allows us to rationalize: i) the different adsorption energies associated to the different chemisorption sites; ii) the quasi degeneracy of B and H adsorption energies; iii) the negligible structural perturbations undergone by THQ when chemisorbed at the T site.

THQ adsorption at HT: The annealing of THQ@Cu(111) up to ~ 385 K implies the dehydrogenation of the four hydroxyl groups to generate the 2,3,5,6-tetraoxyquinone tetra-anion (TOQ) schematically depicted in Figure 3.2.4a, which self-assembles into extended and single-domain islands, as revealed by the inspection of the STM image reported in Fig. 3.2.4b [Lo Cicero et al., 2017]. These islands are characterized by a 4 × 4 periodicity implying an intermolecular distance of 10.2 Å, as revealed by low energy electron diffraction (LEED, see Figure 3.2.4d) and in agreement with the Fast Fourier Transform (FFT) of the STM image (compare Figures 3.2.4b and 3.2.4c). Individual molecular units appear in the STM images as doughnut-like protrusions (see Figure 3.2.5) with a size compatible with that of a single molecule and with an intermolecular distance equal to four times the interatomic copper distance.

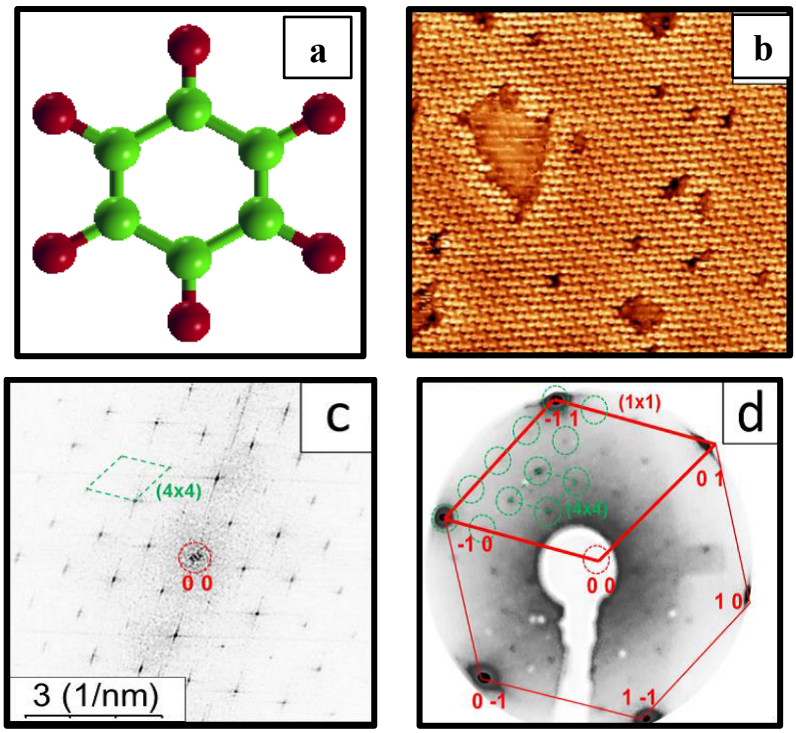

Figure 3.2.4 Schematic representation of the TOQ anion (a); large scale STM image (bias = 0.55 V, I = 37.2 nA) showing the self-assembly of TOQ on Cu(111) after annealing to ~ 385 K (b); corresponding fast Fourier Transform (FFT) image (c); low-energy electron-diffraction pattern (LEED) acquired at an energy of 45 eV on the same sample (d).

The homogeneity in the apparent height of the doughnut-like structures points toward a flat adsorption geometry of the molecules, with the molecular ring parallel to the Cu(111) plane. High-resolution STM images show that additional, apparently triangular, features are present between the doughnuts (see Figure 3.2.5).

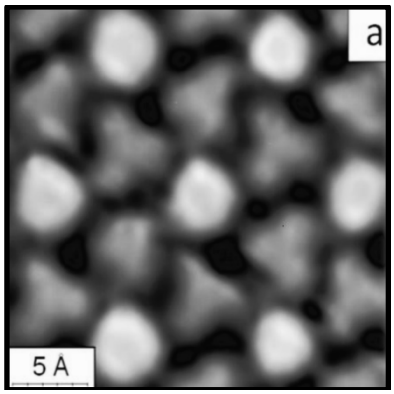

Figure 3.2.5 High-resolution STM image (bias = 0.55 V; I = 37.2 nA) of TOQ tetra-anions assembled on the Cu(111) surface.

Incidentally, these additional features do not appear as triangles if defects are present in the molecular network, thus suggesting that the dominant triangular-shaped structure is present only when it is surrounded by three molecules. Lo Cicero et al. [Lo Cicero et al., 2017] demonstrated that each triangular-shaped structure consists of a tetrameric Cu cluster generated by thermally released Cu_{ad} incorporated in a metal-organic network by TOQ units and comprising a central Cu_{ad} ($^{C}Cu_{ad}$), not involved in any directly interaction with the organic tetraanion, and three peripheral Cu_{ad} ($^{P}Cu_{ad}$), directly bound to $^{C}Cu_{ad}$ as well as to the O TOQ atoms.

Similarly to the modeling of the THQ@Cu(111) at RT, diverse chemisorption sites (T, B, and H) have been considered for TOQ generated on Cu(111) at HT (see Figure 3.2.6). Numerical experiments have been carried out by using the hexagonal p(4 × 4) supercell outlined in the Figure 3.2.6 and by exploiting either the PBE or the PBE-D2 XC functionals. As far as the BZ sampling is concerned, two distinct sets of calculations have been run: the former with a 2 × 2 × 1 ***k***-point mesh; the latter by limiting the BZ sampling at the Γ-point to favor the comparison with data recently published by Lo Cicero et al. [Lo Cicero et al., 2017]. Selected geometrical parameters evaluated at the different chemisorption sites of TOQ@Cu(111) are collected in Tables 3.2.5 and 3.2.6, where selected TOQ BLs and adsorbate–substrate distances are reported, respectively, for different XC functionals and BZ samplings.

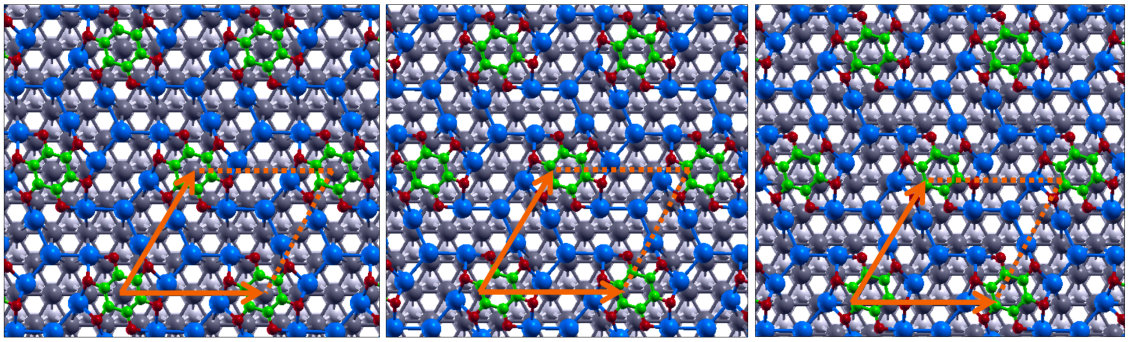

(a) (b) (c)

Figure 3.2.6 Schematic representation of the optimized geometries assumed for the TOQ chemisorption sites on Cu(111): (a) T, (b) B, (c) H. Corresponding unit cells are also displayed. Blue spheres are representative of Cu_{ad}, while the color code of the remaining atomic species is the same of the Figures 1 and 2. Only the first and second layer of the five layer slab representative of the Cu(111) surface are included in the figure. The p(4 × 4) supercell we adopted to optimize geometrical parameters is outlined in orange.

Table 3.2.5 TOQ BLs (Å) at the T, B and H chemisorption sites. The superscript Γ refers to the numerical experiments carried out by limiting the BZ sampling at the Γ point. For B and H chemisorption site average BLs are reported.

	$^{\Gamma}$PBE^{T}	PBE^{T}	PBE-D2^{T}	$^{\Gamma}$PBE^{B}	PBE^{B}	PBE-D2^{B}	$^{\Gamma}$PBE^{H}	PBE^{H}	PBE-D2^{H}
C–C	1.43	1.43	1.42	1.44[a]	1.45[e]	1.43[i]	1.43[m]	1.45[q]	1.44[u]
C–O	1.32	1.32	1.33	1.30[b]	1.29[f]	1.29[j]	1.30[n]	1.29[r]	1.30[v]
Cu_{ad}–O	2.10/2.14	2.10/2.16	2.10/2.16	2.06[c]	2.01[g]	2.04[k]	2.09[o]	2.01[s]	2.00[x]
Cu_{ad}–Cu_{ad}	2.64	2.63	2.64	2.64[d]	2.62[h]	2.58[l]	2.64[p]	2.62[t]	2.54[y]

[a](BL_M = 1.47; BL_m = 1.42); [b](BL_M = 1.32; BL_m = 1.27); [c](BL_M = 2.16; BL_m = 1.95); [d](BL_M = 2.80; BL_m = 2.57)
[e](BL_M = 1.48; BL_m = 1.42); [f](BL_M = 1.31; BL_m = 1.27); [g](BL_M = 2.18; BL_m = 1.94); [h](BL_M = 2.77; BL_m = 2.49)
[i](BL_M = 1.47; BL_m = 1.40); [j](BL_M = 1.33; BL_m = 1.27); [k](BL_M = 2.17; BL_m = 1.89); [l](BL_M = 2.70; BL_m = 2.44)
[m](BL_M = 1.46; BL_m = 1.41); [n](BL_M = 1.31; BL_m = 1.28); [o](BL_M = 2.15; BL_m = 1.98); [p](BL_M = 2.72; BL_m = 2.54)
[q](BL_M = 1.48; BL_m = 1.41); [r](BL_M = 1.32; BL_m = 1.27); [s](BL_M = 2.12; BL_m = 1.93); [t](BL_M = 2.72; BL_m = 2.52)
[u](BL_M = 1.48; BL_m = 1.40); [v](BL_M = 1.32; BL_m = 1.27); [x](BL_M = 2.12; BL_m = 1.91); [y](BL_M = 2.62; BL_m = 2.44)

Theoretical outcomes reported in Table 3.2.5 reveals that the inclusion of dispersion corrections negligibly affect BLs for all the assembled structures, while the opposite is true when the TOQ–Cu(111) distances are considered (see Table 3.2.6). As a matter of fact, even though TOQ tetraanions appear systematically "parallel" to the substrate (independently of the adopted XC functional), the use of the PBE-D2 one is accompanied by a definitely smaller adsorbate–substrate spacing for TOQ@T. Moreover, differently from results obtained by limiting the BZ sampling to the Γ point [Lo Cicero et al., 2017], data herein included for the T chemisorption site stress the presence of two rather than three Cu_{ad}–O distinct BLs, see Figures 3.2.7 and 3.2.8.

Table 3.2.6 TOQ–Cu(111) distances (Å) at the T, B and H chemisorption sites. The superscript Γ refers to the numerical experiments carried out by limiting the BZ sampling at the Γ point. For B and H chemisorption site average internuclear distances are reported.

Atom	$^{\Gamma}$PBE^{T}	PBE^{T}	PBE-D2^{T}	$^{\Gamma}$PBE^{B}	PBE^{B}	PBE-D2^{B}	$^{\Gamma}$PBE^{H}	PBE^{H}	PBE-D2^{H}
C	3.13	3.16	2.85	3.10[a]	3.28[e]	2.98[i]	3.18[m]	3.51[q]	3.23[u]
O	2.95	2.94	2.74	3.02[b]	3.22[f]	2.98[j]	3.02[n]	3.24[r]	3.14[v]
$^{C}Cu_{ad}$	1.92	1.95	1.94	2.02[c]	2.04[g]	1.97[k]	1.93[o]	2.05[s]	2.00[x]
$^{P}Cu_{ad}$	2.09	2.09	2.04	2.08[d]	2.08[h]	2.01[l]	2.08[p]	2.05[t]	1.98[y]

[a](AS_M = 3.16; AS_m = 3.06); [b](AS_M =3.21; AS_m = 2.89); [c](AS_M = 2.03; AS_m = 2.02); [d](AS_M = 2.15; AS_m = 1.94)
[e](AS_M = 3.35; AS_m = 3.13); [f](AS_M = 3.39; AS_m = 2.84); [g](AS_M = 2.08; AS_m = 2.02); [h](AS_M = 2.14; AS_m = 2.02)
[i](AS_M = 3.05; AS_m = 2.90); [j](AS_M = 3.14; AS_m = 2.70); [k](AS_M = 1.98; AS_m = 1.96); [l](AS_M = 2.08; AS_m = 1.94)
[m](AS_M = 3.25; AS_m = 3.14); [n](AS_M = 3.29; AS_m = 2.94); [o](AS_M = 1.94; AS_m = 1.91); [p](AS_M = 2.14; AS_m = 2.03)
[q](AS_M = 3.59; AS_m = 3.40); [r](AS_M = 3.49; AS_m = 3.07); [s](AS_M = 2.11; AS_m = 2.00); [t](AS_M = 2.11; AS_m = 2.00)
[u](AS_M = 3.35; AS_m = 3.08); [v](AS_M = 3.37; AS_m = 2.79); [x](AS_M = 2.06; AS_m = 1.94); [y](AS_M = 2.04; AS_m = 1.95)

More specifically, Lo Cicero et al. [Lo Cicero et al., 2017] found "two O atoms bound to the opposite benzene ring C atoms bind to a single Cu tetramer adatom, while each of the remaining four O atoms in the TOQ molecule establishes two non-equivalent coordination bonds with Cu atoms from different tetramers". The inspection of Figures 3.2.7 and 3.2.8 ultimately indicates a much more symmetric structure when the chemisorption takes place at the T site rather than at the B or H sites.

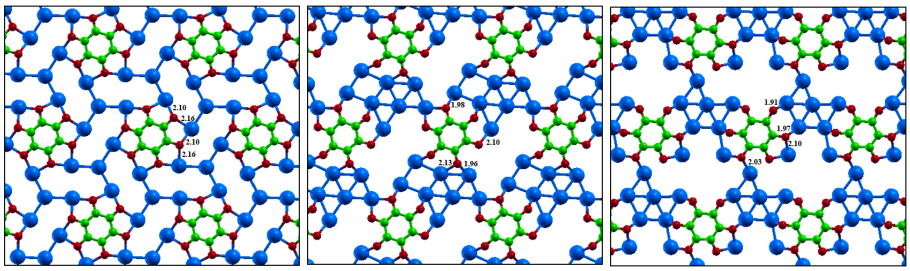

(a) (b) (c)

Figure 3.2.7 Schematic representation of the surface supported metallorganic network generated by the interaction between TOQ tetraanions at the T (a), B (b) and H (c) chemisorption sites on Cu(111). The relaxed substrate is not displayed for the sake of clarity.

The astonishing agreement between STM measurements and the HT simulations generated for the highly symmetric arrangement of TOQ@T (see below) rules definitely out the need of any detailed description of the "disordered" surface supported metal-organic network generated by tetrameric Cu_{ad} clusters and TOQ@B and TOQ@H.

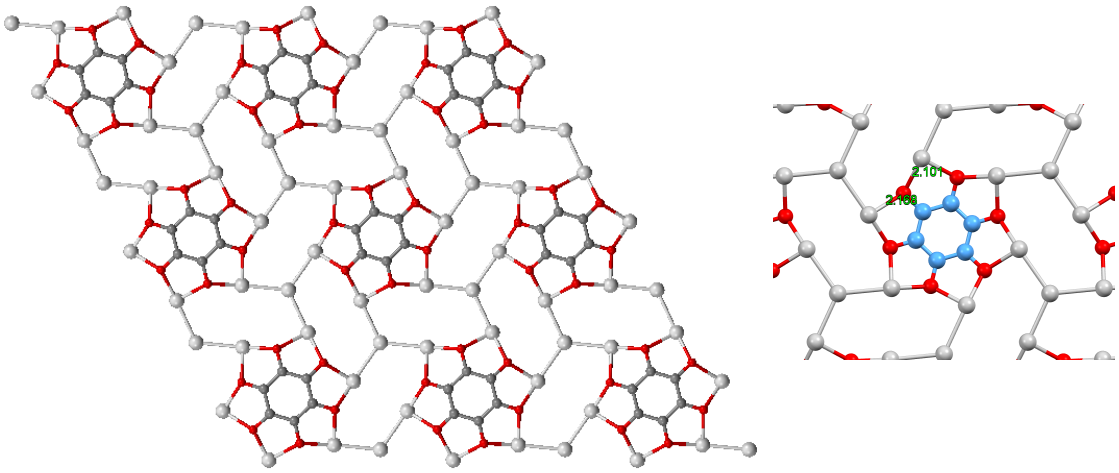

Figure 3.2.8 Schematic representation of the surface supported metallorganic network generated by the interaction between TOQ tetraanions at the T chemisorption site on Cu(111) and tetrameric Cu_{ad} clusters (left). Cu_{ad} nearest neighbors of a single TOQ tetraanion at the T chemisorption site on Cu(111) (right). The relaxed substrate is not displayed for the sake of clarity.

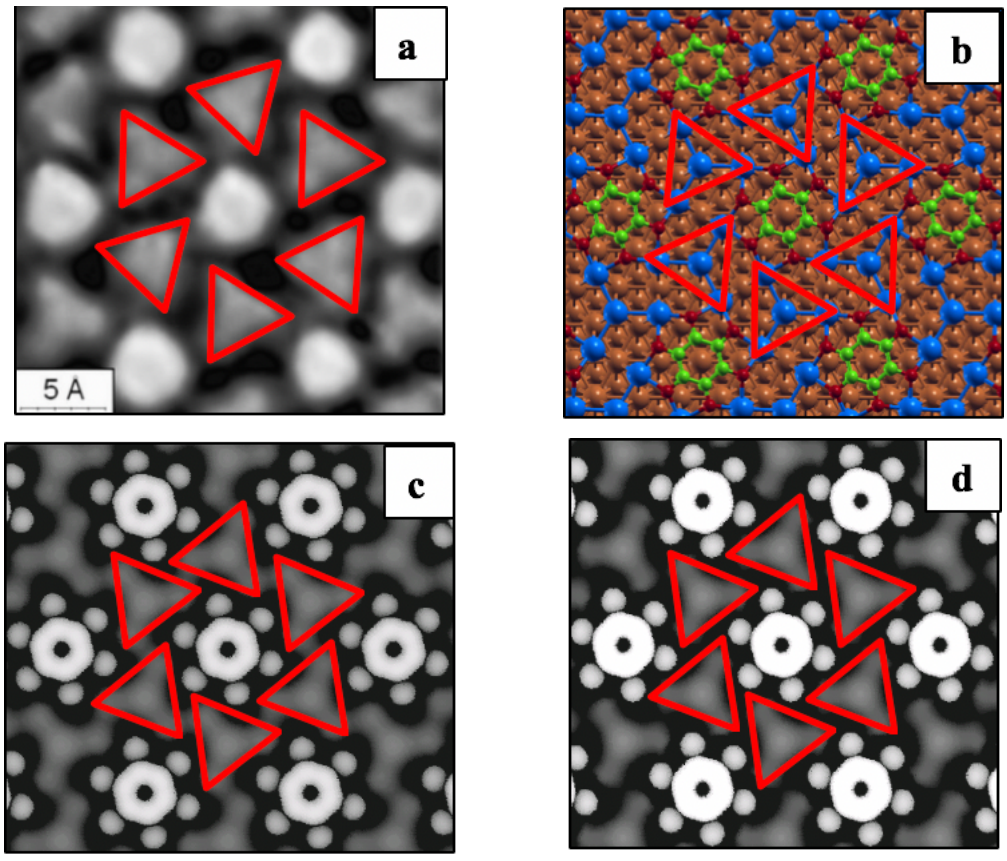

Figure 3.2.9 Experimental (a) and simulated STM images obtained with (c) and without (d) the inclusion of dispersion corrections for TOC@T on Cu(111) at ~110 °C and a bias voltage of V = 0.55 V. The PBE-D2 optimized geometry (b) has been also reported.[9]

[9] The PBE optimized geometry slightly differs from the PBE-D2 one (see Tables 3.2.5 and 3.2.6); nevertheless, the TOQ@T PBE schematic representation is undistinguishable from the PBE-D2 one and for this reason it has not been included in Figure 3.2.9. Analogous considerations hold for TOQ@B and TOQ@H.

STM images of TOQ adsorbed at HT on Cu(111) are compared in Figures 3.2.9 with PBE and PBE-D2 TH simulation for TOQ@T. Relevant differences between PBE and PBE-D2 results concern the higher (lower) brightness of Ph rings (O atoms) when the PBE rather than the PBE-D2 functional is adopted (compare TH simulations in panel c and and d of Figure 3.2.9). Such an evidence is a direct consequence of the overestimated PBE adsorbate-substrate separation (see Table 3.2.6), particularly evident for the Ph carbon atoms. Just for comparison, PBE-D2 optimized structures and corresponding simulated STM images for TOQ@B and TOQ@H are displayed in Figure 3.2.10.

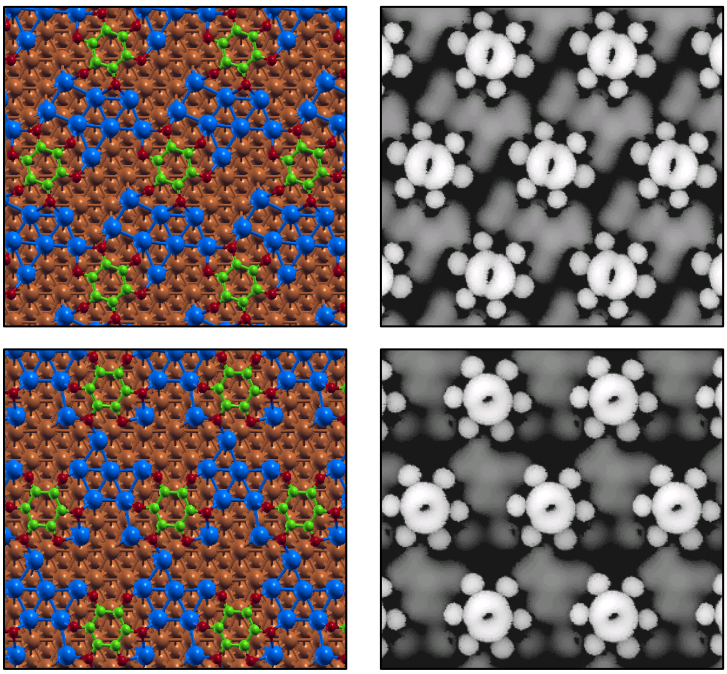

Figure 3.2.10 PBE-D2 optimized geometry of TOC@B (left upper panel) and corresponding TH simulated STM image (right upper panel). PBE-D2 optimized geometry of TOQ@H (left lower panel) and corresponding TH simulated STM images obtained (right lower panel).

In conclusion, we have modelled the chemisorption of the THQ monomer on the Cu(111) surface at different temperatures with and without the inclusion of dispersion corrections by combining STM measurements and periodic DFT calculations. Numerical experiments have been carried out for diverse chemisorption sites, namely top, bridge, and hollow sites. According to the DFT outcomes, the B site is the most favoured for THQ@Cu(111) at LT. Moreover, even though DFT results herein

reported substantially confirm the experimental evidences recently published by Lo Cicero et al. [Lo Cicero et al., 2017] for the THQ 2D pattern annealed at ~110 °C, the use of a BZ richer sampling and the inclusion of dispersion corrections allowed a definitely better agreement between experiment and theory. In particular, the preferred arrangement for THQ@Cu(111) at HT corresponds to the T site of the dehydrogenated TOQ tetraanion directly bound to tetrameric Cu adatoms through oxygen atoms.

Bibliography

Adamo, C.; Barone, V. *J. Chem. Phys.* **1999**, *110*, 6158.

Advances in Polymer Science, vol. 177, Ed. Weder, Ch., Springer, Berlin **2005**.

Allen, F. H.; Kennard, O.; Watson, D. G.; Brammer, L.; Orpen, A. G.; Taylor, R. *J. Chem. Soc., Perkin Trans. 2*, **1987**, *0*, S1.

Ambrosch-Draxl, C.; Majewski, J.; Vogl, P.; Leising, G. *Phys. Rev. B: Condens. Matter* **1995**, *51*, 9668.

Ashcroft, N. W.; Mermin, N. D. *Solid state physics*, Philadelphia: Holt Saunders, **1976**.

Baroni, S.; Giannozzi, P. *American Geophysical Union, Fall Meeting* **2009**.

Basagni, A.; Sedona, F.; Pignedoli, C. A.; Cattelan, M.; Nicolas, L.; Casarin, M.; Sambi, M. *J. Am. Chem. Soc.* **2015**, *137*, 1802.

Basagni, A.; Vasseur, G.; Pignedoli, C.A.; Vilas-Varela, M.; Peña, D.; Nicolas, L.; Vitali, L.; Lobo-Checa, J.; De Oteyza, D. G.; Sedona, F.; Casarin, M.; Sambi, M. *ACSNano* **2016**, *10*, 2644.

Bebensee, F.; Svane, K.; Bombis, C.; Masini, F.; Klyatskaya, S.; Besenbacher, F.; Ruben, M.; Hammer, B.; Linderoth, T. *Chem. Commun.* **2013**, *49*, 9308.

Bebensee, F.; Svane, K.; Bombis, C.; Masini, F.; Klyatskaya, S.; Besenbacher, F.; Ruben, M.; Hammer, B.; Linderoth, T. *Angew. Chem., Int. Ed.* **2014**, *53*, 12955.

Becke, A. D. *Int. J. Quantum. Chem.* **1983**, *23*, 1915.

Becke, A. D. *J. Chem. Phys*. **1986**, *84*, 4524.

Becke, A. D. *J. Chem. Phys.* **1988**a, *88*, 1053.

Becke, A. D. *J. Chem. Phys.* **1988**b, *88*, 2547.

Becke, A. D. *Phys. Rev. A: At. Mol. Opt. Phys.* **1988**c, *38*, 3098.

Betti, M. G.; Gargiani, P.; Mariani, C.; Biagi, R.; Fujii, J.; Rossi, G.; Resta, A.; Fabris, S.; Fortuna, S.; Torrelles, X.; Kumar, M.; Pedio, M. *Langmuir* **2012**, *28*, 13232.

Bloch, F. Z. Physik **1928**, 52, 555.

Bogani, L.; Wernsdorfer, W. *Nat. Mater.* **2008**, *7*, 179.

Born, M.; Oppenheimer, R. *Ann. Phys.* **1927**, *84*, 457.

Bravais, A. *J. Ecole Polytech.* **1850**, *19*, 1.

Brillouin, Léon *Comptes Rendus Hebdomadaires des Séances de l'Académie des Sciences* **1930**, *191*, 292.

Bronner, C.; Björk, J.; Tegeder, P. *J. Phys. Chem. C* **2015**, *119*, 486.

Bunz, U. H. F. *Chem. Rev.* **2000**, *100*, 1605.

Bunz, U. H. F. *Adv. Polym. Sci.* **2005**, *177*, 1.

Callaway, J.; March, N. H. *Solid State Phys.* **1984***, 38*, 135.

Casari, C.S.; Tommasini, M.; Tykwinski, R.R.; Milani, A. *Nanoscale* **2016**, *8*, 4414.

Ceperley, D. M.; Alder, J. B. *Phys. Rev. Lett.* **1980**, *45*, 566.

Chadi, D. J.; Cohen, M. L. *Phys. Rev. B: Condens. Matter* **1973**, *8*, 5747.

Chung, K. H.; Koo, B. G.; Kim, H.; Yoon, J. K.; Kim, J. H.; Kwon, Y. K.; Kahng, S. J. *Phys. Chem. Chem. Phys.* **2012**, *14*, 7304.

Cirera, B.; Zhang, Y.-Q.; Klyatskaya, S.; Ruben, M.; Klappenberger, F.; Barth, J. V. *ChemCatChem* **2013**, *5*, 3281.

Cirera, B.; Zhang, Y.-Q.; Björk, J.; Klyatskaya, S.; Chen, Z.; Ruben, M.; Barth, J. V.; Klappenberger, F. *Nano Lett.* **2014**, *14*, 1891.

Clair, S.; Abel, M.; Porte, L. *Chem. Comm.* **2014**, *50*, 9627.

Cohen, M. L.; Heine, V. *Solid State Physics* 1**970**, *24*, 37.

Cole, L. A.; Perdew, J. P. *Phys. Rev. A: At. Mol. Opt. Phys.* **1982**, *25*, 1265.

Coleman, A. J. *Rev. Mod. Phys.* **1963**, *35*, 668.

Constantin, L. A.; Pitarke, J. M.; Dobson, J. F.; Garcia-Lekue, A.; Perdew, J. P. *Phys. Rev. Lett.* **2008**, *100*, 036401.

Cotts, P. M.; Swager, T. M.; Zhou, Q. *Macromolecules*, **1996**, *29*, 7323.

De Pristo, A. E.; Kress, J. D. *J. Chem. Phys*. **1987**, *86*, 1425.

Di Giovannantonio, M.; El Garah, M.; Lipton-Duffin, J.; Meunier,V.; Cardenas, L.; Fagot Revurat, Y.; Cossaro, A.; Verdini, A.; Perepichka, D. F.; Rosei, F.; Contini, G. *[ACS]Nano* **2013**, *7*, 8190.

Dion, M.; Rydberg, H.; Schröder, E.; Langreth, D. C.; Lundqvist, B. I. *Phys. Rev. Lett.* **2004**, *92*, 246401.

Dirac, P. A. M. *Math. Proc. Cambridge* **1930**, *26*, 376.

Dmitriev, A.; Spillmann, H.; Lin, N.; Barth, J. V.; Kern, K. *Angew. Chem.* **2003**, *115*,

2774.

Dong, L.; Gao, Z.; Lin, N. *Prog. Surf. Sci.* **2016**, *91*, 101.

Dreuw, A.; Head-Gordon, M. *J. Am. Chem. Soc*. **2004**, *126*, 4007.

Dreuw, A.; Weisman, J. L.; Head-Gordon, M. *J. Chem. Phys*. **2003**, *119*, 2943.

Ecija, D.; Vijayaraghavan, S.; Auwärter, W.; Joshi, S.; Seufert, K.; Aurisicchio, C.; Bonifazi, D.; Barth, J. V. *ACSNano* **2012**, *6*, 4258.

Eichhorn, J.; Heckl, W. M.; Lackinger, M. *Chem. Commun.* **2013**, *49*, 2900.

Eichhorn, J.; Nieckarz, D.; Ochs, O.; Samanta, D.; Schmittel, M.; Jerzy Szabelski, P.; Lackinger, M. *ACSNano* **2014**, *8*, 7880.

Ernzerhof, M.; Scuseria, G. *J. Chem. Phys.* **1999**, *110*, 5029.

Evarestov, R. A.; Smirnov, V. P. *Phys. Status Solidi* **1983**, *119*, 9.

Ewald, P. *Ann. Phys.* **1921**, *369*, 253.

Fan, Q.; Gottfried, J. M.; Zhu, J. *Acc. Chem. Res.* **2015**, *48*, 2484.

Fan, Q.; Liu, L.; Dai, J.; Wang, T.; Ju, H.; Zhao, J.; Kuttner, J.; Hilt, G.; Gottfried, J. M.; Zhu, J. *ACSNano* **2018**, *12*, 2267.

Fermi, E. *Rend. Accad. Naz. Lincei* **1927**, *6*, 602.

Fermi, E. *Z. Physik* **1928**, *48*, 73.

Feynman, R. P. *Eng. Sci.* **1960**, *23*, 22.

Fiolhais, C.; Nogueira, F.; Marques M. (Eds.) *A Primer in Density Functional Theory*, Springer-Verlag Berlin, Heidelberg **2003**

Fortuna, S.; Gargiani, P.; Betti, M. G.; Mariani, C.; Calzolari, A.; Modesti, S.; Fabris, S. *J. Phys. Chem. C* **2012**, *116*, 6251.

Franc, G.; Gourdon, A. *Phys. Chem. Chem. Phys.* **2011**, *13*, 14283.

Francis, G. P.; Payne, M. C. *J. Phys.: Condens. Matter* **1990**, *17*, 1643.

Gantenbein, M.; Wang, L.; Al-jobory, A. A.; Ismael, A. K.; Lambert, C. J.; Hong, W.; Bryce, M. R. *Sci. Rep.* **2017**, *7*, 1794.

Gao, H.-Y.; Wagner, H.; Zhong, D.; Franke, J.-H.; Studer, A.; Fuchs, H. *Angew. Chem. Int. Ed.* **2013**, *52*, 4024.

Geerlings, P.; De Proft, F.; Langenaeker, W. *Chem. Rev*. **2003**, *103*, 1793.

Giannozzi, P.; Baroni, S.; Bonini, N.; Calandra, M.; Car, R.; Cavazzoni, C.; Ceresoli, D.; Chiarotti, G. L.; Cococcioni, M.; Dabo, I.; Dal Corso, A.; de Gironcoli, S.; Fabris, S.; Fratesi, G.; Gebauer, R.; Gerstmann, U.; Gougoussis, C.; Kokalj, A.; Lazzeri, M.; Martin-Samos, L.; Marzari, N.; Mauri, F.; Mazzarello, R.; Paolini, S.; Pasquarello, A.;

Paulatto, L.; Sbraccia, C.; Scandolo, S.; Sclauzero, G.; Seitsonen, A. P.; Smogunov, A.; Umari, P.; Wentzcovitch, R. M. *J. Phys. Condens. Matter*, **2009**, *21*, 395502.

Gilbert T. L., *Phys. Rev. B: Condens. Matter* **1975**, *12*, 2111.

Giannozzi, P.; Andreussi, O.; Brumme, T.; Bunau, O.; Buongiorno Nardelli, M.; Calandra, M.; Car, R.; Cavazzoni, C.; Ceresoli, D.; Cococcioni, M.; Colonna, N.; Carnimeo, I.; Dal Corso, A.; de Gironcoli, S.; Delugas, P.; DiStasio, R. A. Jr.; Ferretti, A.; Floris, A.; Fratesi, G.; Fugallo, G.; Gebauer, R.; Gerstmann, U.; Giustino, F.; Gorni, T.; Jia, J.; Kawamura, M.; Ko, H.-Y.; Kokalj, A.; Küçükbenli, E.; Lazzeri, M.; Marsili, M.; Marzari, N.; Mauri, F.; Nguyen, N. L.; Nguyen, H.-V.; Otero-de-la-Roza, A.; Paulatto, L.; Poncé, S.; Rocca, D.; Sabatini, R.; Santra, B.; Schlipf, M.; Seitsonen, A. P.; Smogunov, A.; Timrov, I.; Thonhauser, T.; Umari, P.; Vast, N.; Wu, X.; Baroni, S. *J. Phys.: Condens. Matter* **2017**, *29*, 465901.

Gill, P.; Murray, W.; Wright, M. *Practical optimization*, Academic Press, London, **1981**.

González-Moreno, R.; Sánchez-Sánchez, C.; Trelka, M.; Otero, R.; Cossaro, A.; Verdini, A.; Floreano, L.; Ruiz-Bermejo, M.; García-Lekue, A.; Martín-Gago, J. Á.; Rogero, C. *J. Phys. Chem. C* **2011**, *115*, 6849.

Gottfried, J. M.; Flechtner, K.; Kretschmann, A.; Lukasczyk, T.; Steinrück, H.-P. *J. Am. Chem. Soc.* **2006**, *128*, 5644.

Görling, A.; Levy, M. *Phys. Rev. B: Condens. Matter* **1993**, *47*, 105.

Görling, A.; Levy, M. *Phys. Rev. A: At. Mol. Opt. Phys.* **1994**, *50*, 196.

Gourdon, A. *Angew. Chem. Int. Ed.* **2008**, *47*, 6950.

Grill, L.; Dyer, M.; Lafferentz, L.; Persson, M.; Peters, M. V.; Hecht, S. *Nat. Nanotechnol.* **2007**, *2*, 687.

Grimme, S. *J. Chem. Phys.* **2006**a, *124*, 34108.

Grimme, S. *J. Comput. Chem.* **2006**b, *27*, 1787.

Gritsenko, O. V.; Schipper, P. R. T.; Baerends, E. J. *Chem. Phys. Lett*. **1999**, *302*, 199.

Grumelli, D.; Wurster, B.; Stepanow, S.; Kern, K. *Nat. Commun*. **2013**, *4*, 2904.

Gruning, M.; Gritsenko, O. V.; van Gisbergen, S. J. A.; Baerends, E. J. *J. Chem. Phys*. **2001**, *114*, 652.

Guam, C.-Z.; Wang, D.; Wan, L.-J. *Chem. Comm.* **2012**, *48*, 2943.

Gunnarsson, O.; Lundqvist, B. *Phys. Rev. B: Condens. Matter* **1976**, *13*, 4274.

Günther, J. R.; Oswald, H.-R. *Bull. Inst. Chem. Res., Kyoto Univ.* **1975**, *53*, 249.

Gutzler, R.; Perepichka, D. F. *J. Am. Chem. Soc.* **2013**, *135*, 16585.

Hashmi, A. S. K.; Hutchings, G. J. *Angew. Chem., Int. Ed.* **2006**, *45*, 7896.

Hepburn, J.; Scoles, G.; Penco, R. *Chem. Phys. Lett.* **1975**, *36*, 451.

Hohenberg, P.; Kohn, W. *Phys. Rev. B*.: *Condens. Matter* **1964**, *136*, 864.

Joannopoulos, J. D.; Cohen, M. L. *J. Phys. C* **1973**, *6*, 1572.

Jones II, L.; Schumm, J. S.; Tour, J. M. *J. Org. Chem.* **1997**, *62*, 1388.

Kastner, C.; Susarova, D. K.; Jadhav, R.; Ulbricht, C.; Egbe, D. A. M.; Rathgeber, S.; Troshin, P. A.; Hoppe, H. *J. Mater. Chem.* **2012**, *22*, 15987.

Kittel, C. *Introduction to Solid State Physics - Eighth Edition*, John Wiley & Sons, **2005**.

Klappenberger, F.; Hellwig, R.; Du, P.; Paintner, T.; Uphoff, M.; Zhang, L.; Lin, T.; Abedin Moghanaki, B.; Paszkiewicz, M.; Vobornik, I.; Fujii, J.; Fuhr, O.; Zhang, Y.-Q.; Allegretti, F.; Ruben, M.; Barth, J. V. *Small* **2018**, *14*, 1704321.

Kleinman, L.; Lee, S. *Phys. Rev. B: Condens. Matter* **1988**, *37*, 4634.

Kokalj, A. *J. Mol. Graphics Model* **1999**, *17*, 176.

Kokalj, A.; Causà M. *Scientific visualization in computational quantum chemistry, Proceedings of High Performance Graphics Systems and Applications European*, Workshop, Bologna, Italy, **2000**.

Kokalj, A.; Dal Corso, A.; de Gironcoli, S.; Baroni, S. *Surf. Sci.* **2002**, *507*, 62.

Kovačević, N.; Kokalj, A. *Corros. Sci.* **2013**, *73*, 7.

Kretschmann, A.; Walz, M.-M.; Flechtner, K.; Steinrück, H.-P.; Gottfried, J. M. *Chem. Comm.* **2007**, *6*, 568.

Kubo, Y.; Nishiyabua, R.; Jamesc T. D. *Chem. Comm.* **2015**, *51*, 2005.

Kudernac, T.; Lei, S.; Elemans, J. A. A. W.; De Feyter, S. *Chem. Soc. Rev.* **2009**, *38*, 402.

Kumar, A.; Chhatwal, M.; Chandra Mondal, P.; Singh, V.; Kumar Singh, A.; Cristaldi, D. A.; Gupta, R. D.; Gulino, A. *Chem. Comm.* **2014**, *50*, 3783.

Iikura, H.; Tsuneda, T.; Yanai, T.; Hirao, K. *J. Chem. Phys*. **2001**, *115*, 3540.

Israelachvili, J. N. *Intermolecular and Surface Forces*, Academic, London, **1992**.

Jiang, J-X.; Su, F.; Trewin, A.; Wood, C. D.; Campbell, N. L.; Niu, H.; Dickinson, C.; Ganin A.Y.; Rosseinsky, M. J.; Khimyak, Y. Z.; Cooper, A. I. *Angew. Chem. Int. Ed.* **2007**, *46*, 8574.

Koch, W.; Holthausen, M. C. *Neural Netw.* **2001**, *3*, 294.

Kohn, W.; Sham, L. J. *Phys. Rev. A: At. Mol. Opt. Phys.* **1965**, *140*, 1133.

Kristyan, S.; Pulay, P. *Chem*. *Phys. Lett*. **1994**, *229*, 175.

Landau, L. D.; Lifshitz, E. M. *Quantum Mechanics,* Pergamon Press, **1965**.

Langreth, D. C.; Mehl, M. J. *Phys. Rev. B: Condens. Matter* **1983**, *28*, 1809.

Lee, C.; Yang, W.; Parr, R. G. *Phys. Rev. B: Condens. Matter* **1988**, *37*, 785.

Lee, K.; Murray, É. D.; Kong, L.; Lundqvist, B. I.; Langreth, D. C. *Phys. Rev. B: Condens. Matter* **2010**, *82*, 081101.

Leeuwen, R. V.; Baerends, E. J. *Phys. Rev. A: At. Mol. Opt. Phys.* **1994**, *49*, 2421.

Lehn, J. M. *Supramolecular Chemistry*, VCH, **1995**

Levy, M. *Proc. Natl. Acad. Sci. USA*, **1979**, *76*, 6062.

Li, Y.; Xu, L.; Liu, H.; Li, Y. *Chem. Soc. Rev.* **2014**, *43*, 2572.

Lide, D. R. *CRC Handbook of Chemistry and Physics*, 89th ed. (Internet Version); CRC Press/Taylor and Francis: Boca Raton, **2009**.

Lieb, E. H.; Simon, B. *Phys. Rev. Lett*. **1973**, *31*, 681.

Lieb, E. H. *Rev. Mod. Phys.* **1981**, *53*, 603.

Lipton-Duffin, J. A.; Ivasenko, O.; Perepichka, D. F.; Rosei, F. *Small* **2009**, *5*, 592.

Liu, W.; Ruiz, V. G.; Zhang, G. X.; Santra, B.; Ren, X.; Scheffler, M.; Tkatchenko, A. *New J. Phys.* **2013**, *15*, 053046.

Liu, C.; Yang, B.; Tyo, E.; Seifert, S.; DeBartolo, J.; von Issendorff, B.; Zapol, P.; Vajda, S.; Curtiss, L. A. *J. Am. Chem. Soc.* **2015**, *137*, 8676.

Liu, J.; Chen, Q.; Xiao, L.; Shang, J.; Zhou, X.; Zhang, Y.; Wang, Y.; Shao, X.; Li, J.; Chen, W.; Xu, G. Q.; Tang, H.; Zhao, D.; Wu, K. *ACSNano*, **2015**, *6*, 6305.

Lo Cicero, M.; Della Pia, A.; Riello, M.; Colazzo, L.; Sedona, F.; Betti, M. G.; Sambi, M.; De Vita, A.; Mariani, C. *J. Chem. Phys.* **2017**, *147*, 214706.

Lotgering, F. K. *J. Inorg. Nucl. Chem.* **1959**, *9*, 113.

London, F. W. *Z. Phys*. **1930**, *63*, 245.

London, F. *Trans. Faraday Soc.* **1937**, *33*, 8b.

Lovat, G.; Forrer, D.; Abadia, M.; Dominguez, M.; Casarin, M.; Rogero, C.; Vittadini, A.; Floreano, L. *Nanoscale*, **2017**, *9*, 11694.

Löwdin, P. O. *J. Chem. Phys.* **1950**, *18*, 365.

Lu, G.; Yang, H.; Zhu, Y.; Huggins, T.; Ren, Z. J.; Liu, Z.; Zhang, W. *J. Mater. Chem. A* **2015**, *3*, 4954.

Marbach, H. *Acc. Chem. Res.*, **2015**, *48*, 2649.

March, N. H. *Phys Lett A*. **1986**, *113*, 476.

Margenau, H. *Rev. Mod. Phys.* **1939**, *11*,1.

Martin, R. E.; Diederich, F. *Angew. Chem. Int. Ed.* **1999**, *38*, 1350.

Marzari, N.; Vanderbilt, D.; De Vita, A.; Payne, M. C. *Phys. Rev. Lett.* **1999**, *82*, 3296.

Methfessel, M. P. A. T.; Paxton, A.T. *Phys. Rev. B: Consens. Matter* **1989**, *40*, 3616.

Monkhorst, H. J.; Pack, J. D. *Phys. Rev. B: Condens. Matter* **1976**, 13, 5188.

On-Surface Synthesis. *Proceedings of the International Workshop On-Surface Synthesis*, École des Houches, Les Houches 25-30 May 2014. Ed. Gourdon, A., Springer International Publishing, **2016**.

On-Surface Synthesis II. *Proceedings of the International Workshop On-Surface Synthesis*, San Sebastián, 27-30 June 2016. Eds. De Oteyza, D. G.; Rogero, C., Springer International Publishing, **2018**.

Ortiz, M.; Yu, C.; Jin, Y.; Zhang, W. *Top. Curr. Chem. (Z)* **2017**, *375*, 69.

Parr, R. G.; Yang, W. *Density Funtional Theory of Atoms and Molecules*, Oxford University Press NY, **1989**.

Pauli, W. Jr. *Z. Phys*. **1925**, *31*, 765.

Pauling, L. *The Nature of the Chemical Bond*, Cornell University Press, 3rd edn., **1960**.

Perdew, J. P.; Zunger, A. *Phys. Rev. B: Condens. Matter* **1981**, *23*, 5048.

Perdew, J. P. *Phys. Rev. Lett.* **1985**, *55*, 1665.

Perdew, J. P.; Wang, Y. *Phys. Rev. B: Condens. Matter,* **1986**a, *33*, 8800.

Perdew, J. P. *Phys. Rev. B: Condens. Matter*, **1986**b, *33*, 8822.

Perdew, J. P.; Wang, Y. *Phys. Rev. B: Condens. Matter,* **1989**, *40*, 3399.

Perdew, J. P.; Wang, Y. *Phys. Rev. B: Condens. Matter*, **1992**, *45*, 13244.

Perdew, J. P.; Burke, K.; Ernzerhof, M. *Phys. Rev. Lett.* **1996**, *77*, 3865.

Perdew, J. P.; Staroverov, V. N.; Tao, J.; Scuseria, G. E. *Phys. Rev. A: At. Mol. Opt. Phys.* **2008**, *78*, 052513.

Perdew, J. P.; Ruzsinszky, A.; Constantin, L. A.; Sun, J.; Csonka, G. I. *J. Chem. Theory Comput.* **2009**, *5*, 902.

Perepichka, D. F.; Rosei, F. *Angew. Chem., Int. Ed.* **2007**, *46*, 6006.

Perepichka, D. F.; Rosei, F. *Science* **2009**, *323*, 216.

Pham, T. A.; Song, F.; Nguyen, M.; Li, Z.; Studener, F.; Stöhr, M. *Chem. – Eur. J.* **2016**, *22*, 5937.

Phillips, J. C. *Phys. Rev.* **1958**, *112*, 685.

Píš, I.; Ferrighi, L.; Nguyen, T. H.; Nappini, S.; Vaghi, L.; Basagni, A.; Magnano, E.; Papagni, A.; Sedona, F.; Di Valentin, C.; Agnoli, S.; Bondino, F. *J. Phys. Chem. C* **2016**, *120*, 4909.

Plas, J.; Ivasenko, O.; Martsinovich, N.; Lackingercd, M.; De Feyter, S. *Chem. Comm.* **2016**, *52*, 68.

Polak, E. *Computational methods in optimization*, Academic Press, New York, **1971**.

Rayleigh, J. W. S. *Theory of Sound. I*, 2nd Ed., London: Macmillan, **1894**.

Riley, K. F.; Hobsonm M. P.; Bence, S. J. *Mathematical Methods for Physics and Engineering*, Third Edition, Cambridge University Press, **2006**.

Rosseinsky, M. *Microporous Mesoporous Mater.* **2004**, *73*, 15.

Ruiz, V. G.; Liu, W.; Tkatchenko, A. *Physical Review B: Condens. Matter* **2016**, *93*, 035118.

Sasaki, S.; Yamamoto, T.; Kanbara, T.; Morita, A. *J. Polym. Sci., Part B: Polym. Phys.* **1992**, *30*, 293.

Savin, A. *In Recent Developments and Applications of Modern Density Functional Theory.* Ed. Seminario J. M., Elsevier, Amsterdam, **1996**.

Schipper, P. R. T.; Gritsenko, O. V.; Baerends, E. J. *Theor. Chim. Acta*. **1997**, *98*, 16.

Schore, N. E. *Chem. Rev.* **1988**, *88*, 1081.

Schrödinger, E. *Ann. Phys.* **1926**a, *79*, 109.

Schrödinger, E. *Ann. Phys.* **1926**b, *79*, 361.

Schrödinger, E. *Ann. Phys.* **1926**c, *79*, 489.

Schrödinger, E. *Ann. Phys.* **1926**d, *79*, 734.

Schrödinger, E. *Ann. Phys.* **1926**e, *80*, 437.

Schrödinger, E. *Phys. Rev.* **1926**f, *28*, 1049.

Schrödinger, E. *Naturwissenshaften*, **1926**g, *14*, 664.

Schumm, J. S.; Pearson, D. L.; Tour, J. M. *Angew. Chem. Int. Ed.* **1994**, *33*, 1360.

Slater, J. C.; Kirkwood, J. G. *Phys. Rev.* **1931**, *37*, 682.

Sonogashira, K. *J. Organomet. Chem.* **2002**, *653*, 46.

Steinhauser, M. O. *Computational Multiscale Modeling of Fluids And Solids - Theory And Applications*, Springer, **2008**.

Stepanow, S.; Lingenfelder, M.; Dmitriev, A.; Spillmann, H.; Delvigne, E.; Lin, N.; Deng, X.; Cai, C.; Barth, J. V.; Kern, K. *Nat. Mater.* **2004**, *3*, 229.

Stephens, P. J.; Devlin, F. J.; Chabalowski, C. F.; Frisch, M. *J. Phys. Chem.* **1994**, *98*, 11623.

Stone, A. J. *The Theory of Intermolecular Forces*, Second Edition, Oxford University Press, **2013**.

Sun, Q.; Yu, X.; Bao, M.; Liu, M.; Pan, J.; Zha, Z.; Cai, L.; Ma, H.; Yuan, C.; Qiu,

X.; Xu, W. *Angew. Chem. Int. Ed.* **2018**, *57*, 1.

Swager, T. M. *Acc. Chem. Res.* **2008**, *41*, 1181.

Szabo, A.; Ostlund, N. S. *Modern Quantum Chemistry*: *Introduction to Advanced Electronic Structure Theory*, Dover Publications, **1996**.

Tao, J.; Perdew, J. P.; Staroverov, V. N.; Scuseria, G. E. *Phys. Rev. Lett.* **2003**, *91*, 146401.

Teller, E. *Rev. Mod. Phys*. **1962**, *34*, 627.

Tersoff, J.; Hamann, D. R. *Phys. Rev. B: Condens. Matter* **1985**, *31*, 805.

Teter, M. P.; Payne, M. C.; Allan, D. C. *Phys. Rev. B: Condens. Matter* **1989**, *40*, 12255.

Thomas, L. H. *Proc. Cambridge Philos. Soc*. **1927**, *23*, 542.

Toffoli, D.; Stredansky, M.; Feng, Z.; Balducci, G.; Furlan, S.; Stener, M.; Ustunel, H.; Cvetko, D.; Kladnik, G.; Morgante, A.; Verdini, A.; Dri, C.; Comelli, G.; Fronzoni, G.; Cossaro, A. *Chem. Sci.* **2017**, *8*, 3789.

Tonigold, K.; Grob, A. *J. Chem. Phys.* **2010**, *132*, 224701.

Toyoda, K.; Hamada, I.; Lee, K.; Yanagisawa, S.; Morikawa, Y. *J. Chem. Phys.* **2010**, *132*, 134703.

Tozer, D. J.; Handy, N. C. *J. Chem. Phys*. **1998**, *109*, 10180.

Tran, B. V.; Pham, T. A.; Grunst, M.; Kivala, M.; Stöhr, M. *Nanoscale*, **2017**, *9*, 1805.

Tschinke, V.; Ziegler, T. *Can. J. Chem.* **1989**, *67*, 460.

Tsuneda, T.; Suzumura, T.; Hirao, K. *J. Chem. Phys.* **1999**, *111*, 5656.

Tsuneda, T.; Hirao, K. *Phys. Rev. B: Condens. Matter* **2000**, *62*, 15527.

Tsuneda, T.; Kamiya, M.; Morinaga, N.; Hirao, K. *J. Chem. Phys.*, **2001**, *114*, 6505.

Tsuneda T, *Density Functional Theory in Quantum Chemistry*, Springer Japan, 2014.

van Gisbergen, S. J. A.; Kootstra, F.; Schipper, P. R. T.; Gritsenko, O. V.; Snijders, J. G.; Baerends, E. J. *Phys. Rev. A: At. Mol. Opt. Phys.* **1998**, *57*, 2556.

Ullmann, F.; Bielecki, J. *Chem. Ber.* **1901**, *34*, 2174.

Unsöld, A. *Z. Physik* **1927**, *43*, 563.

Vanderbilt, D. *Phys. Rev. B: Condens. Matter* **1990**, *41*, 7892.

Venkataraman, L.; Klare, J. E.; Nuckolls, C.; Hybertsen, M. S.; Steigerwald, M. L. *Nat. Lett.* **2006**, *442*, 904.

Verdini, A.; Shinde, P.; Montanari, G. L.; Suran-Brunelli, S. T.; Caputo, M.; Di Santo, G.; Pignedoli, C. A.; Floreano, L.; Passerone, D.; Goldoni, A. *Chem. Eur. J.* **2016**, *22*, 14672.

Vitos, L.; Ruban, A.V.; Skriver, H. L.; Kollár, J. *Surf. Sci.* **1998**, *411*, 186.

Vosko, S. H.; Wilk, L.; Nusair, N. *Can. J. Phys.* **1980**, *58*, 1200.

Wang, Y.; Sun, Q.; Fan, K.; Deng, J. *Chem. Phys. Lett.* **2001**, *334*, 411.

Weder, C.; Sarwa, C.; Montali, A.; Bastiaansen, C.; Smith, P. *Science* **1998**, *279*, 835.

Weizsäcker, C. F. *Z. Phys*. **1935**, *96*, 341.

Wigner, E. *Phys. Rev*. **1934**, *46*, 1002.

Williams, H. L.; Chabalowski, C. F. *J. Phys. Chem*. **2001**, *105*, 646.

Yin, M. T.; Cohen, M. L. *Phys. Rev. B: Condens. Matter* **1982**, *25*, 7403.

Zhang, Y.Q.; Kepčija, N.; Kleinschrodt, M.; Diller, K.; Fischer, S.; Papageorgiou, A. C.; Allegretti, F.; Björk, J.; Klyatskaya, S.; Klappenberger, F.; Ruben, M.; Barth, J. V. *Nat. Commun.* **2012**, *3*, 1286.

Zhao, Y.; Truhlar, D. G. *Theor. Chem. Accounts* **2008**, *120*, 215.

Ziegler, T. *Chem. Rev*. **1991**, *91*, 651.